Diurnal Cycle of Precipitation Over Tropical and Midlatitude Lands: GCM Inter-Comparison

Cheng Tao[1], Shaocheng Xie[*,1], Hsi-Yen Ma[1], Peter Bechtold[2], Zeyu Cui[3], Paul A. Vaillancourt[4], Kwinten Van Weverberg[5, 6], Yi-Chi Wang[7], May Wong[8], Jing Yang[4], Guang J. Zhang[9], In-Jin Choi[10], Shuaiqi Tang[11], Jiangfeng Wei[12], Wen-Ying Wu[1], Meng Zhang[1], J. David Neelin[13], Xubin Zeng[14]

[1]*Lawrence Livermore National Laboratory, Livermore, CA, USA*

[2]*European Centre for Medium-Range Weather Forecasts, Reading/Bologna/Bonn, UK/Italy/Germany*

[3]*Tsinghua University, Beijing, China*

[4]*Environment and Climate Change Canada, Dorval, Québec, Canada*

[5]*Department of Geography, University of Ghent, Ghent, Belgium*

[6]*Met Office, Exeter, UK*

[7]*Research Center for EnvironmentalChanges, Academia Sinica, Taipei, Taiwan*

[8]*National Center for Atmospheric Research, Boulder, CO, USA*

[9]*Scripps Institution of Oceanography, La Jolla, CA, USA*

[10]*Korea Institute of Atmospheric Prediction Systems, Seoul, South Korea*

[11]*Pacific Northwest National Laboratory, Richland, WA, USA*

[12]*Nanjing University of Information Science and Technology, Nanjing, China*

[13]*University of California Los Angeles, CA, USA*

[14]*University of Arizona, Tucson, AZ, USA*

Submit to *Q J R Meteorol. Soc.*

**Corresponding author address*: Shaocheng Xie, Atmospheric, Earth, and Energy Division (L-103), Lawrence Livermore National Laboratory, Livermore, CA 94550.
E-mail: xie2@llnl.gov

Abstract

Diurnal precipitation is a fundamental mode of variability that climate models have difficulty in accurately simulating. Here the diurnal cycle of precipitation (DCP) in participating climate models from the Global Energy and Water Exchanges' DCP project is evaluated over tropical and midlatitude lands. Common model biases such as excessive precipitation over the tropics, too frequent light-to-moderate rain, and the failure to capture propagating convection in the central U.S. still exist. Over the central U.S., the issues of both too weak rainfall intensity and the incorrect timing of DCP in climate runs is well improved in their hindcast runs with initial conditions from Numerical Weather Prediction analyses. But the improvement is minimal over the central Amazon. Incorporating the role of the large-scale environment in convective triggering processes helps resolve the phase-locking issue in many models where precipitation often incorrectly peaks near noon due to maximum insolation over land. Allowing air parcels to be lifted above the boundary layer improves the simulation of nocturnal precipitation which is often associated with the propagation of mesoscale systems. Including convective memory in cumulus parameterizations acts to suppress light-to-moderate rain and promote intense rainfall; however, it also weakens the diurnal variability. Simply increasing model resolution (with cumulus parameterizations still used) cannot fully resolve the biases of low-resolution climate models in DCP. The hierarchy modeling framework from this study is useful for identifying the missing physics in models and testing new development of model convective processes over different convective regimes.

1. Introduction

The diurnal cycle of precipitation (DCP) is one of the most fundamental modes of atmospheric variability (Yang and Slingo, 2001). It significantly affects the surface energy budget and surface temperature (Dai et al. 1999). DCP is considered a benchmark for climate models, with which multiple aspects of the simulated precipitation, such as total amount, frequency, intensity, and duration, can be effectively evaluated (Covey et al. 2016). Several key features of the precipitation diurnal cycle have been discovered from observational studies: the diurnal cycle is stronger over land with precipitation peaking in late-afternoon or at midnight; the diurnal amplitude over land is stronger in summer than in winter; the diurnal cycle over ocean is relatively weak with the maximum precipitation typically occurring in the morning (e.g., Dai 2006; Dai and Trenberth, 2004; Dai et al. 2007; Yang and Slingo, 2001; Nesbitt and Zipser 2003; Kikuchi and Wang, 2008; Covey et al. 2016).

General Circulation Models (GCMs) for weather forecasts and climate simulations have for decades exhibited difficulties in modeling the diurnal variation in precipitation, particularly over land. Tao et al. (2022) and Tang et al. (2021) examined the latest GCMs from the Coupled Model Intercomparison Project phase 6 (CMIP6, Eyring et al. 2016) and found that the simulated diurnal cycle is substantially improved in the multi-model mean of CMIP6 models compared with that of CMIP5. Tao et al. (2022) also indicated that while DCP over ocean and coastal ocean are fairly well captured by CMIP6 models, the simulated diurnal cycle over land and coastal land continues showing large biases and model spread. In general, common model deficiencies in reproducing the rainfall diurnal cycle include the too frequent convection triggering at reduced intensity, the too early precipitation onset time, and missing the nocturnal precipitation peak associated with elevated convection and propagating mesoscale convective systems (MCSs) (e.g.,

Yang and Slingo, 2001; Dai 2006; Covey et al. 2016; Xie et al. 2019; Fiedler et al. 2020; Ma et al. 2021; Tang et al. 2021&2022; Tao et al. 2022).

The major challenges for GCMs to simulate the DCP well are primarily associated with the shortcomings and deficiencies in representing the processes that control sub-diurnal phenomena like convection and organized convective phenomena like MCSs. Previous studies have demonstrated that DCP can be substantially improved through development of advanced parameterizations (Rio et al. 2009; Park, 2014; Wang et al. 2021; Xie et al. 2019). For example, Xie et al. (2019) suggested that nocturnal precipitation peak and the eastward propagation of convection downstream of the Rockies and over the adjacent Great Plains could be better captured with a new convective trigger, as demonstrated using the Department of Energy's (DOE's) Energy Exascale Earth System Model (E3SM) Atmosphere Model version 1 (EAMv1) (Rasch et al. 2019; Xie et al. 2018). This new physically based convective trigger incorporates a dynamic CAPE (dCAPE) constraint (Xie and Zhang 2000) to suppress daytime convection and an Unrestricted Launch Level (ULL) (Wang et al. 2015) to capture mid-level elevated convection. The simulation of the DCP can also be improved by increasing model resolution to the convection permitting scale. A recent study by Ma et al. (2022) demonstrated that the global storm-resolving models (GSRMs) with horizontal resolutions of ~ 2-5 km convincingly exhibit superior performance in simulating the DCP compared to models with horizontal resolutions of ~ 25 km or coarser.

The recent GEWEX Global Atmospheric System Studies (GASS) Diurnal Cycle of Precipitation intercomparison project (GASS-DCP, https://portal.nersc.gov/project/capt/diurnal/) was organized to better understand what key processes control the diurnal and sub-diurnal variation of precipitation and to identify the deficiencies and missing physics in current GCMs through a hierarchy of modeling approach. Processes associated with DCP are investigated and

diagnosed among different models under a multi-scale modeling framework including single column models (SCMs)/Cloud-Resolving Models (CRMs), Cloud Permitting Models (CPMs), and GCMs using observations over different climate regimes. Earlier findings from a multi-year long-term SCM intercomparison are documented in Tang et al. (2022). These long-term SCM simulations, which are less constrained by the specified large-scale forcing compared to traditional SCM case studies, are able to reproduce many common errors in DCP shown in their parent GCMs. The model errors in simulating DCP are primarily due to deficiencies in their deep convection parameterizations. Tang et al. (2022) suggested that additional constraints in the convective triggering function, as well as unified treatment of turbulence, shallow, and deep convection could help delay the precipitation peak for afternoon precipitation over land while the key to simulate the nocturnal peak is to allow elevated convection to be captured as indicated in Xie et al. (2019). The latter suggests parameterization of mid-level elevated convection is needed in GCMs.

The present study summarizes our analysis on DCP simulated from the participating GCMs in the GASS-DCP. Unlike SCMs, GCMs contain complete interactions between model dynamics and physics, allowing the evaluation of the GCM's skill in simulating DCP over different climate regimes. Our goal here is to provide an assessment of the participating models' capability in simulating DCP over tropical and mid-latitude lands, and to identify the missing physics in GCMs and gain more insights into model errors through a hierarchical model approach that includes both climate simulations and short-term weather hindcasts. The hindcast approach follows Phillips et al. (2004), Williams et al. (2013), and Ma et al. (2015; 2021) with models initiated with Numerical Weather Prediction (NWP) analysis data so that GCMs can be linked to the highly time-resolved field data collected by the U.S. DOE Atmospheric Radiation Measurement (ARM) program. Physical processes that are critical for GCMs to better capture the rainfall diurnal cycle are

explored by comparing the results of models in different versions or with different physical parameterizations. In addition, the impacts of model resolution on the diurnal cycle will also be discussed by connecting results from convection-permitting model intercomparison projects such as DYAMOND (Dynamics of the Atmospheric general circulation Modeled on Non-hydrostatic Domains, Satoh et al. 2019; Stevens et al. 2019).

The paper is organized as the follows. Section 2 introduces the participating models and the designed experiments. The simulated characteristics of the mean precipitation and its global and regional features are documented in section 3. The DCP at two ARM sites is evaluated in section 4. Summary and discussions are given in section 5.

2. Experiment design, participating models and observations

2.1 Experiment design

Two types of numerical modeling experiments are included in this study: (1) an eight-year climate simulation, and (2) a series of 5-day hindcasts covering several selected field campaigns. To provide robust statistics of the participating GCMs' capability in simulating the DCP, eight-year (2011-2018) AMIP simulations are conducted with prescribed National Centers for Environmental Prediction (NCEP) Optimally Interpolated weekly sea surface temperature (SST) and sea ice fraction. The atmospheric and land initial conditions are coming from previous multi-year runs where the atmosphere and land states are fully spun-up.

The short-term hindcasts, initialized every day at 00Z covering selected field campaign periods during the ARM Plains Elevated Convection at Night Experiment (PECAN) (1 June 2015 – 15 July 2015) (Geerts et al., 2017) and Observations and Modeling of the Green Ocean Amazon (GOAmazon) dry season (1 September – 10 October 2014) (Martin et al. 2016), are designed to

build connection between GCMs and in-situ ARM observations. The initial conditions for atmospheric state variables in the short-term hindcasts are from the fifth generation European Center for Medium-range Weather Forecast (ECMWF) atmospheric reanalysis (ERA5, Hersbach et al. 2020) for most models except for the CMCGEM that uses initial conditions from the Canadian Global Deterministic Prediction System (Buehner et al. 2015). SST and sea ice are prescribed with NCEP Optimally Interpolated weekly SST and sea ice or with the Operational Sea Surface Temperature and Sea Ice Analysis (OSTIA) system (Good et al. 2020) for UMGA7 and UMGA8 models. The duration of each hindcast is 5-day long (120 hours). To avoid initial shock from a foreign reanalysis, our analysis on hindcasts only focuses from 24 to 120 h lead time (Day 2 to Day 5). With the hindcast approach, the model simulations will not drift too far away from the observed large-scale state, and most biases can be largely attributed to model parameterizations (Xie et al., 2012; Ma et al., 2013, 2014, 2015, 2018). Therefore, results from the hindcasts can be applied to identify missing physics and deficiencies in representing atmospheric physics in the models and provide more insights into future parameterization improvement.

2.2 Participating models

In total, nine GCMs participated in the multi-year AMIP-style climatology runs and eight GCMs participated in the short-term hindcasts in this intercomparison project. Table 1 lists the basic information of each of the participating models, with detailed information about their model physical parameterizations documented in Tables 2 and 3. The participating models were developed for various scientific applications including weather forecasts and climate simulations over regional and global scales. Models from operational weather forecast and modeling research centers (e.g., CMCGEM, ECMWF-IFS, UMGA7, UMGA8, and MPAS) typically have much finer

resolutions in both the horizontal (15 – 40 km) and vertical (55 - 137 levels) than climate models (e.g., CAM6, E3SMv2, and TaiESM1), which run at 100km in the horizontal and 30 – 72 levels in the vertical. Note that CMCGEM and ECMWF-IFS use a slightly coarser horizontal resolution (39 km and 60 km, respectively) when they are used for the multi-year AMIP climate simulations, but their resolutions are still finer than those of the climate models. Despite the finer resolutions used in the weather models, they still cannot resolve convection. So, cumulus parameterizations are used in all the participating models for representing shallow and deep convection.

In addition to the differences in model resolutions, these models also differ in the representations of physical processes including turbulence, cloud microphysics, and shallow and deep convection. This is particularly true between weather and climate models. Nevertheless, there are some similarities among them, specifically for those having the same origin, such as CAM6, E3SM, and TaiESM1, which were all branched from CAM5 with modifications. The atmospheric physical parameterization in CAM6 is similar to that in E3SM, since they have gone through very similar physical parameterization updates in turbulence, shallow convection, and cloud microphysical schemes. The major differences in these two models are in 1) vertical resolution: 72 levels in E3SMv2 vs. 32 levels in CAM6 and 2) parameter setting for tunable parameters related to cloud and convection. Unlike CAM6 and E3SM which include significant updates in their atmospheric physics from CAM5, TaiESM1 only made some changes in convective trigger for deep convection and kept turbulence, cloud microphysics, and shallow convection the same as CAM5 as shown in Tables 2 and 3.

One common feature for all participating models is that they all use the mass flux approach with a Convective Available Potential Energy (CAPE)-based trigger and closure for deep convection schemes, which is critical for modeled DCP, although the implementation of these

technical details varies from model to model. More specifically, CAM6, E3SMv2 and TaiESM1 all applied the deep convection scheme developed from Zhang and McFarlane (1995) (ZM thereafter). ECMWF-IFS and MPAS share many similarities in the deep convection scheme from Tiedtke (1989) and Bechtold et al. (2014). The mass flux schemes described in Kain and Fritsch (1990) and Gregory and Rowntree (1990) as well as their variants are used in CMCGEM and UMGA.

The convective trigger controls when and where convection occurs in the model and is a key for capturing the DCP. There are large differences in how convection is triggered in these models. Besides positive CAPE that is required by all models, additional constraints also need to be met for convection onset. For example, a threshold of CAPE (>70 J/kg) is set in CAM6-CTL for convection onset. E3SMv2 implements a dynamical CAPE constraint (dCAPE) (Xie and Zhang 2000) and an Unrestricted Launch Level (ULL) (Wang et al. 2015) (dCAPE-ULL) to prevent CAPE from being released spontaneously and allow air parcels to be lifted above boundary layer for mid-level convection (Xie et al. 2019), in addition to the positive CAPE trigger. The ULL method is also applied in TaiESM1 along with convective inhibition (CIN) for convection initiation (Wang et al. 2015). Similarly, ECMWF-IFS introduced a moisture-convergence term in its convective closure (Becker et al. 2021), which implicitly affects its convection onset. It also searches for unstable levels up to 300 hPa that allows elevated convection to be detected. CMCGEM recently made significant updates to its package of convective parameterizations (McTaggart-Cowan et al. 2019a&b, 2020), namely the introduction of a low-CAPE (mid-level) convection scheme and the introduction of a Lagrangian framework for convective initiation. UMGA8 introduces convective memory through implementing a prognostic entrainment scheme in its convective trigger. Given the importance of the convective trigger in DCP, several models

212 performed sensitivity tests by changing their convective triggering functions. For instance, a
213 slightly revised dCAPE-ULL trigger (Cui et al. 2021) is tested in CAM6-Trig; the dilute-CAPE
214 based trigger used in CAM6-CTL (and E3SMv1) is tested in E3SMv2-CAPETrig; UMGA8
215 introduces convective memory in its convective trigger with other settings similar to that of
216 UMGA7. By comparing the results of these sensitivity tests, we can explore the impact of different
217 convective triggering processes on the simulation of DCP in GCMs.

218 As shown in Table 1, in total, seven GCMs have performed both the eight-year climate
219 runs and the 5-day hindcasts. Comparisons between these two types of experiments from the same
220 model will provide hints on whether the biases of GCMs in simulating the DCP are most likely
221 attributed to errors from the large-scale circulation and surface conditions or those from the
222 physical parametrizations. Results from climate runs and hindcasts are analyzed and evaluated
223 using various observational data sets as summarized in Table 4. Discussions of the model results
224 will generally follow the order from low-resolution GCMs (CAM6-CTL, CAM6-Trig, E3SMv2,
225 E3SMv2-CAPETrig, TaiESM1) to GCMs from the weather forecast and research centers with
226 much finer resolutions (CMCGEM, ECMWF-IFS, UMGA7&8, MPAS).

227

228 *2.3 Observations*

229 Due to differences in retrieval algorithm, gap-filling and other aspects of data product
230 creation, differences among observational data sets for precipitation must be carefully considered
231 when using for model comparison. Our selection of observations is limited by the requirement of
232 sub-daily frequency for direct DCP comparison; while for the background comparisons to
233 climatology, we include observational data sets that have only daily and longer timescales as well.
234 The primary data sets used for model comparison are:

- Global Precipitation Climatology Project (GPCP, Adler et al. 2003) monthly products version 2.3 for annual mean distribution and GPCP 1 Degree Daily (1DD) precipitation dataset version 1.3 for daily mean distribution.
- Climate Prediction Center (CPC) Morphing technique (CMORPH, Joyce et al. 2004) bias-corrected product version 1.0 for daily mean distribution and diurnal cycle. We use the hourly CMORPH with a spatial resolution of 0.25 degree.
- The Global Precipitation Measurement (GPM) Integrated Multi-satellitE Retrievals for GPM (IMERG, Huffman et al. 2019) data product for daily mean distribution and diurnal cycle. The IMERG provides 30-min precipitation rates with coverage from 60^{o}S to 60^{o}N in 0.1 degree.
- The Tropical Rainfall Measuring Mission (TRMM, Huffman et al. 2007) 3B42 version 7 data for diurnal cycle which has 3-hourly precipitation rates from 50^{o}S to 50^{o}N in 0.25 degree.
- The ARM variational analysis (VARANAL) products to evaluate the DCP at the ARM Southern Great Plains site (SGP) and the Manacapuru site for the GOAmazon field campaign (MAO). VARANAL uses ground-based radar measurements to represent the rainfall average over a domain comparable to a GCM grid box: a ~ 3^o×3^o domain at SGP (Tang et al. 2019; Xie et al. 2004) and a domain with ~110 km radius at MAO (Tang et al. 2016).

Data from simulations and observations were all interpolated to 1^o×1^o degree resolution using conserved method.

3. Overall performance over the globe

In this section, we will focus on the eight-year (2011-2018) AMIP-style climatology runs with global coverage to evaluate the overall performance of nine GCMs including CAM6-CTL, CAM6-Trig, CMCGEM, ECMWF-IFS, E3SMv2, E3SMv2-CAPETrig, TaiESM1, UMGA7 and UMGA8 (climate runs in Table 1). Model data is saved every 3 hours. The potential impact of model physics on the simulated precipitation distributions and diurnal cycles will also be discussed by comparing results from models with different parameterizations or in different model versions.

3.1 Mean precipitation

Figure 1 displays the annual mean GPCP estimated precipitation, and the bias from AMIP simulations. The spatial correlations (CORR) and root-mean-square errors (RMSE) between the GCMs and GPCP are also given in the figure to quantify model performance. Several common model biases are noted across the GCMs. For example, they tend to produce excessive precipitation over large portions of the tropics but less precipitation over the central U.S. and South America compared to observations, consistent with the results of Coupled Model Intercomparison Project Phase 6 (CMIP6) models (Tang et al. 2021). Overall, the performance of ECMWF-IFS is better than other GCMs in simulating the annual mean precipitation (Fig. 1h), with the highest CORR (0.94) and the lowest RMSE (0.87). The dry bias shown in most climate models over the central US and South America is quite low in ECMWF-IFS. It is noted that UMGA7 also shows smaller error over these two regions compared to other participating models, however, it produces the largest wet bias over tropical oceans. CMCGEM and UMGA8 also indicate a good skill over the central US, but they both show large dry bias over the Amazon region. Similar results are also noted using CMORPH and IMERG for model comparison (not shown).

The overall impact of the dCAPE-ULL convective trigger on the annual mean precipitation is small as demonstrated by the similar distribution of mean precipitation errors between CAM6-CTL and CAM6-Trig and between E3SMv2 and E3SMv2-CAPETrig. However, the use of the dCAPE-ULL trigger has different impacts on the mean precipitation in CAM6 and E3SM. With the new trigger, E3SMv2 shows an overall better result than E3SMv2-CAPETrig with some encouraging improvements in South America, especially in reducing the Amazonia dry biases (Fig. 1d&e). In contrast, CAM6-Trig (Fig. 1c) shows slightly larger errors in the mean precipitation than CAM6-CTL (Fig. 1b). Although TaiESM1 was also branched from CAM5 and used ZM for deep convection, it shows larger biases and smaller CORR compared to CAM6 and E3SMv2, indicating that other physical processes and their interactions with deep convection also impact mean precipitation. The convective memory introduced in UMGA8 does not change the mean precipitation errors in UMGA7 much. While UMGA8 shows some improvements over South Africa and the tropical Indian Ocean, it produces a larger dry bias over the Amazon basin compared with that in UMGA7 (Figs. 1i&j).

3.2 Frequency and amount of precipitation

As shown in Figure 1, the majority of precipitation error occurs in the tropics. On the other hand, the warm and dry bias over the central U.S. in the summer is one of the most conspicuous model biases that has persisted in many generations of climate models. To further explore the regional features, the precipitation intensity distributions of the annual mean in the tropics (30^{o}S – 30^{o}N) and over the summer contiguous U.S. (CONUS) are examined in Figure 2a and 2b, respectively.

Different from that of mean precipitation, discrepancies among various observational data sets are noted in the precipitation intensity distributions, which indicates certain level of uncertainty. Particularly, GPCP tends to under-represent high intensity rain rates while underrepresenting low rain rates compared with that of CMORPH and IMERG in the tropics, consistent with the findings in previous studies (Martinez-Villalobos and Neelin, 2021; Martinez-Villalobos et al. 2022). Overall, compared to the observations, GCMs tend to overpredict the frequency of rainfall rates between 0.5-2.0 mm/day while underestimating rainfall rates greater than 15 mm/day over both the tropics and the summer CONUS. Note that different from other GCMs, both UMGA7 and UMGA8 tend to overpredict the frequency of very intense precipitation (> 25-30 mm/day) over the tropics. This is related to the excessive precipitation produced in the tropical and subtropical oceans in these two models. In addition, the modeled total precipitation distribution exhibits a large spread in its probability density functions (PDFs). Different from the tropics, where a strong bimodal distribution is simulated in most GCMs, the modeled precipitation shows large precipitation frequency between 0.5 and 5 mm/day over the CONUS.

Models with different versions or parameterizations show some differences in the precipitation intensity distributions over both of the examined regions but the differences are in general more evident in the tropics than over the CONUS. In the tropics, the dCAPE-ULL trigger in E3SMv2 helps reduce the overestimation of frequency of rain rates in E3SMv2-CAPETrig between 1.0 and 10 mm/day, consistent with Xie et al. (2019). The reduction of light-to-moderate rain is mainly attributed to the dCAPE method applied in E3SMv2 which effectively suppresses the convection as found in Zhang and Mu (2005) and Xie et al. (2019). Similarly, the overestimation of the precipitation frequency at the bin of [1.0-10 mm/day] in CAM6-CTL is largely reduced in CAM6-Trig with the dCAPE-ULL trigger. This is also the case for UMGA8

compared to UMGA7, indicating that including convective memory acts to suppress light-to-moderate rain likely because information from previous convection helps maintain and enhance the follow-up development of convection. Having convective memory in UMGA8 also promotes intense rainfall events as UMGA8 has more intense precipitation than UMGA7, consistent with cloud-resolving simulations (Daleu et al., 2020). Overall, the impact of new changes in CAM6-Trig, E3SMv2 and UMGA8 on the precipitation frequency distributions is only notable in the light-moderate rain range, as the corresponding distributions are pretty similar to that of CAM6-CTL, E3SMv2-CAPETrig and UMGA7, respectively, for intense rain.

3.3 Global distribution of diurnal precipitation

Figure 3 shows the comparison of the time phase (color) and amplitude (color density) of the first diurnal harmonic of total precipitation between three different observations (e.g., CMORPH, IMERG and TRMM) and model simulations over the tropics (20^{o}S-20^{o}N). The modeled precipitation over the oceans tends to peak a few hours earlier (closer to midnight) than that observed in most of the participating models, with the exception of ECMWF-IFS which closely reproduces the observed widespread morning peaks. The diurnal precipitation peaks over the Maritime continent region are also well captured by ECMWF-IFS, which reproduces the observed late-evening peaks over land and the transition to morning peaks toward the coasts and open oceans (Fig. 3f).

Over the tropical continents, including Africa, South America, and South Asia, the observed late-evening to midnight precipitation peaks are in general captured by CMCGEM (Fig. 3i) and ECMWF-IFS (Fig. 3j). Overall, the diurnal peak phase is similar for CAM6-CTL (Fig. 3d), E3SMv2-CAPETrig (Fig. 3g) and TaiESM1 (Fig. 3h), where the diurnal precipitation peaks are

nearly phase-locked to maximum insolation over tropical Africa and tropical South America. The similarity in simulating the diurnal timing is largely attributed to the same deep convection scheme (ZM) used in these three models. The CAPE (applied in CAM6-CTL and E3SMv2_CAPETrig) or CIN (TaiESM) triggers used in these models are so strongly tied to solar radiation that they cannot prevent CAPE from being released spontaneously after it is generated by the solar heating. The phase-locking behaviors are also noted for UMGA7 (Fig. 3k) and UMGA8 (Fig. 3l), where they both simulate morning peaks over most of the tropical land areas. The dCAPE-ULL trigger implemented in CAM6-Trig (Fig. 3e) and E3SMv2 (Fig. 3f) effectively breaks the phase-locking behaviors associated with the CAPE trigger used in CAM6-CTL, E3SMv2-CAPETrig and TaiESM1, and delays the precipitation peak at the noon or early-afternoon to between late-evening and midnight or shortly after. However, over most of the tropical land regions, the peak time in CAM6-Trig and E3SMv2 occurs a few hours earlier than the observations.

The observed and modeled phase and amplitude of diurnal precipitation over the summer CONUS are displayed in Figure 4. Overall, the performance of participating models on the DCP is worse over the CONUS than over the tropics. Common model biases, including the too early daytime precipitation peak over the Southeast U.S. and the missing of nocturnal precipitation peak over the central U.S., are noted in CAM6-CTL (Fig. 4d). These model biases are notably reduced in CAM6-Trig (Fig. 4e) with the dCAPE-ULL trigger. The use of the dCAPE-ULL trigger in E3SMv2 also helps capture the nocturnal precipitation peak missed by E3SMv2-CAPETrig. But the late-afternoon peak over the eastern U.S., which is correctly simulated in E3SMv2-CAPETrig, is delayed to midnight in E3SMv2 (Figs. 4f&g). This is in contrast to the significant improvement of the new trigger in simulating diurnal timing phases over CONUS as shown in Xie et al. (2019). Further analyses indicate that the re-tuning of several adjustable parameters used in ZM during the

E3SMv2 development has a negative impact on its simulated DCP (Golaz et al. 2022). This issue is being addressed by the E3SM team for its next version of the model. Different from CAM6-CTL and E3SMv2-CAPETrig, TaiESM1 successfully captures the nocturnal precipitation peak over the U.S. Great Plains (Fig. 3h). This is mainly attributed to the ULL method implemented in TaiESM1, which is key to capturing the nocturnal elevated convection (Xie et al. 2019; Wang et al. 2015). In the meantime, however, the bias of too early precipitation peaks during the daytime still persists in TaiESM1 such as over the southern and southeastern U.S., indicating that the main effect of dCAPE trigger is to delay daytime precipitation.

While CMCGEM is able to produce the observed late-afternoon peak over the eastern and southeastern U.S., it misses the nocturnal precipitation maximum over the central U.S. (Fig. 4i). The performance of ECMWF-IFS over the summer CONUS is generally worse than that over the tropics. The diurnal precipitation seems to peak a few hours later over the southeastern U.S. compared to all three observations (Fig. 4j). Overall, the distributions of the summertime diurnal timing phase and amplitude are similar between UMGA7 (Fig. 4k) and UMGA8 (Fig. 4l), where both models simulate a diurnal peak a few hours earlier (around noon) than the observations over the eastern and southeastern U.S. This suggests that the convective memory added in UMGA8 has little impact on the simulated DCP. It should be noted that here we only focus on the diurnal harmonics. However, to fully represent the daily variations, harmonics in semidiurnal and higher frequencies are also needed. Detailed analysis on the modeled DCP at selected ARM sites will be discussed later in section 4.

3.4 Propagation of convection over the U.S. Great Plains

The diurnal cycle of observed surface precipitation over the U.S. Great Plains is featured with a primary peak between midnight and early morning during the warm season (e.g., Dai et al., 1999; Jiang et al., 2006; Klein et al., 2006). This nocturnal precipitation is usually linked to the propagating convection systems into the Great Plains, which originates from the lee of the Rocky Mountains during the afternoon (e.g., Jiang et al., 2006; Xie et al., 2014; Geerts et al., 2017). Figure 5 illustrates the mean diurnal and longitudinal distribution of precipitation (averaged from 35^{o} to 45^{o}N) from observations and GCMs over the central U.S. during the summertime. Here, a clear eastward propagation of convection is noted in all three observations (CMORPH, IMERG and TRMM) with a sharp pickup in precipitation starting at 1500-1800 LST over 105^{o}W (Figs. 5a-c). The precipitation associated with deep convection then moves eastward to the Great Plains with increased intensity, peaking at 2100-0000 LST over 100^{o}W. The results are in general similar among various observational data sets.

Overall, most of the participating models tend to underestimate the precipitation amounts, consistent with the long-standing dry and warm bias in GCMs over the Great Plains during the warm seasons (Klein et al., 2006; Ma et al. 2018). In addition, the observed propagation features are generally absent in GCMs. This is consistent with Ma et al. (2022) which demonstrated that the multi-model means (MMM) from both "high"-resolution global models with typical resolution of ~50 km and "standard"-resolution global models with typical resolution of ~100 km fail to simulate the propagating convective in the central U.S. On the other hand, the UMGA models (both UMGA7 and UMGA8) show some capability to simulate the propagation of convection over the Great Plains but with a greater propagation speed. For instance, the UMGA8-simulated precipitation peaks at around 1500 LST over 105^{o}W, moves eastward to the Great Plains and peaks at around 0000 LST and 0300 LST over 100^{o}W and 95^{o}W, respectively (Fig. 5l). While CAM6-

Trig (Fig. 5e), E3SMv2 (Fig. 5f), TaiESM1 (Fig. 5h) and ECMWF-IFS (Fig. 5j) also shows the signal of propagation of convection eastward towards the Great Plains, the rain peak time is always a few hours later compared to the observations.

4. Diurnal cycle of precipitation at the ARM SGP and GOAmazon sites

In this section, the simulated DCP from both AMIP-style climatology runs and short-range hindcast runs will be evaluated at two ARM sites of distinct environmental conditions: 1) the SGP site, representative of midlatitude land conditions with upper-level westerlies and a dry free troposphere, and 2) the MAO site, representative of tropical rain-forest conditions with warm, moist air in the lower and middle troposphere.

4.1 The ARM SGP site

a. Composite means

The composite mean DCP from climate runs and the ARM continuous forcing data set (Xie et al. 2004, Tang et al. 2019), averaged for eight summer seasons (June-August, 2011-2018) at the SGP, are shown in Figure 6a. As expected, the DCP from the ARM observations presents a nocturnal peak after midnight and a daytime minimum at around noon. In general, the simulated precipitation intensity is too weak in all participating models. For CAM6-CTL and E3SMv2-CAPETrig, particularly, the diurnal precipitation maximum is less than 1.5 mm/day compared with 5.0 mm/day from the ARM observations. In addition, most of the participating GCMs have difficulties in capturing the ARM-observed nocturnal precipitation maximum, consistent with the results of long-term SCM tests in Tang et al. (2022). The modeled precipitation either shows a diurnal maximum around noon or displays a double-peak diurnal pattern. The timing of DCP is

only reasonably simulated by CAM6-Trig, E3SMv2 and ECMWF-IFS, although the modeled peak is still one or two hours later than the ARM observations.

The better simulated diurnal phase in CAM6-Trig, E3SMv2, and ECMWF-IFS could be attributed to a relatively more accurate representation of the interactions between their convective triggering processes and the large-scale environment and the use of unrestricted launch level in these models. This is consistent with Tang et al. (2022), which indicated that models with the capability of allowing convection to be triggered above the boundary layer can better simulate the observed nocturnal precipitation. As discussed in Xie et al. (2019), the dCAPE-ULL trigger, employed in both CAM6-Trig and E3SMv2, contains a dynamic constraint related to the large-scale temperature and moisture advection for suppressing daytime convection and the ULL allowing instability to be captured above the boundary layer for nocturnal elevated convection. The combination of these two approaches allows CAM6-Trig and E3SMv2 to capture the diurnal phase of precipitation at the SGP site. The observed nocturnal peak is also well simulated by ECMWF-IFS, which is probably because ECMWF-IFS incorporates moisture convergence in its closure (which has implicit impact on its trigger) and searches for unstable levels up to 300 hPa. The physics behind the dCAPE-ULL trigger and the ECMWF-IFS trigger and closure are similar. It is interesting that while TaiESM1 is able to capture the nocturnal precipitation peak, due to the ULL trigger, it produces a secondary peak near 1300 LST as well. This again indicates that the CIN trigger in TaiESM1 cannot effectively suppress spurious early afternoon convection in the model since CIN is also small during the day as a result of solar heating.

Results from the 5-day hindcasts, averaged over Day 2 to Day 5 hindcast lead time, during the PECAN field campaign (June 01 – July 15, 2015) are shown in Figure 6b. With more realistic large-scale conditions enforced in the hindcasts, the participating models produce much stronger

462 precipitation in the hindcast runs than their climate runs. Similar results are also noted in the SCM
463 intercomparison project where the simulated diurnal amplitude is greater in SCMs compared to
464 GCMs (Tang et al. 2022). This suggests that the problem with too weak diurnal amplitude in the
465 climate runs may result from the errors in the large-scale circulations and surface conditions (e.g.,
466 soil moisture) and the interaction between convection and its environment. Additionally, the
467 observed nocturnal peak is well captured by almost all the models in the hindcast runs except for
468 E3SMv2-CAPETrig, which continues to produce a diurnal peak in the late afternoon similar to its
469 climate runs. Although CAM6-CTL and CAM6-Trig did not participate in the hindcast
470 experiment, we expect the simulated DCP in CAM6-CTL to be comparable with that in E3SMv2-
471 CAPETrig given their similarities. In the meantime, most of the participating models largely
472 overestimate the precipitation during the day and show a secondary peak between 1300 and 1800
473 LST. The only exception to this issue is E3SMv2 which nicely reproduces the observed diurnal
474 features. The overall better performance of E3SMv2 in both short-term hindcasts and long-term
475 climate runs suggests that the dCAPE-ULL trigger can effectively help capture DCP over the SGP
476 region.

477 It is noted that CMCGEM, ECMWF-IFS, and MPAS performed the hindcast runs with
478 very high horizontal resolutions (< 20 km). CMCGEM shows a much better performance in the
479 hindcasts than its climate simulations. The improvement could be attributed to both the increased
480 resolution from climate runs (39 km) to hindcasts (15 km) and the better described large-scale
481 environments and initial conditions in the hindcast runs. But this seems not the case for ECMWF-
482 IFS and MPAS. Although the ARM-observed nocturnal precipitation maximum is captured by the
483 hindcast runs of ECMWF-IFS, the simulated precipitation between 1500 and 2100 LST is too
484 strong compared with that observed. Similarly, the hindcast runs of MPAS also show a diurnal

precipitation maximum in the late afternoon. The similarities between these two models could be partially because the deep convection scheme used in the 15-km MPAS runs is based on the New Tiedtke scheme in WRF, which in turn, is very similar to the scheme employed in ECMWF-IFS. This suggests that the biases of low-resolution climate models in capturing the DCP may not be fully resolved by simply increasing model resolutions as long as cumulus parameterizations are used in the model. To better capture the diurnal phase, a convection permitting resolution is needed. As demonstrated in Ma et al. (2022), models with resolutions between 2.5 km to 5 km used in the DYAMOND project do show a clear improvement in capturing the diurnal phase compared to those in the CMIP6 GCMs.

For the UMGA models, UMGA8 shows considerably weaker diurnal variability than UMGA7 in both simulations, especially the hindcast runs. To further explore this, statistics of the precipitation duration for rainfall events are also examined. It is found that with convective memory, rainfall events tend to last longer in UMGA8 than UMGA7 in the hindcast runs (not shown), reducing the diurnal variability in Fig. 6b. Overall, both models show difficulties in capturing the DCP at SGP with double peaks shown in their simulated DCP (one in the afternoon and one around the midnight) although the observed nocturnal peak is reasonably captured in their hindcast simulations.

b. Individual nocturnal rainfall events

The DCP based on the composites of a few weeks could be biased from a few strong precipitation events. Here, simulations from the 5-day hindcast runs are further examined through day-to-day comparisons with the ARM observations. Specifically, we focus on the observed

507 nocturnal precipitation days, defined as having a peak rain rate greater than 1 mm/day, and rain
508 peak time between 0000 and 0700 LST, following Tang et al. (2022).

509 Figure 7 illustrates the observed and simulated peak rain rate (mm/day) and rain peak time
510 (LST) for each day during the PECAN field campaign. In total, 12 nocturnal precipitation days are
511 selected from the ARM observations. Overall, CMCGEM compares best to the observations. Ten
512 out of 12 (~ 83%) observed nocturnal precipitation days are correctly simulated as nocturnal
513 precipitation days in CMCGEM, with one day having peak rain rate less than 1 mm/day (Jun-06)
514 and one day having rain peak time at around 2300 LST (Jun-11). The nocturnal precipitation
515 regime is also reasonably well captured by ECMWF-IFS and TaiESM1, which correctly reproduce
516 three quarters of the identified nocturnal precipitation days from the ARM observations. The hit
517 rate to reproduce the ARM-observed nocturnal precipitation days is the lowest in E3SMv2-
518 CAPETrig (~33%) while it doubles in E3SMv2 (~67%). The significant improvement from
519 E3SMv2-CAPETrig to E3SMv2 in the day-to-day comparison is consistent with the results from
520 the above composite means. Common features are noted among the participating models for the
521 days that are recognized as nocturnal precipitation days in the ARM observations but are not in
522 the models. In the majority of the wrong cases from the hindcast runs, the nocturnal precipitation
523 is generally captured by the models (i.e., maximum rain rate > 1 mm/day between 00-07 LST) but
524 the rain peak time occurs between the late afternoon and early evening.

525

526 *4.2 The ARM GOAmazon site*

527 a. Composite means

528 Figure 8a shows the mean DCP from climate runs averaged for eight dry seasons
529 (September-October, 2011-2018) and ARM observations (September-October 2014) (Tang et al.

2016) at the Manacapuru site in the central Amazon (MAO) of Brazil. Consistent with previous studies, the ARM observations show a diurnal precipitation peak in the early afternoon at around 1400 LST. Overall, most of the participating models show a better performance in capturing the DCP, including both diurnal phase and amplitude, at the ARM MAO site than that at the SGP site. Note that local-driven afternoon convection is the dominant precipitation system in the dry season at the ARM MAO site (e.g., Tang et al., 2016). When including propagating convective systems mostly occurring in the wet season and at other times of the day, model performance will likely degrade (Tang et al., 2022).

The common model bias of too early precipitation peaks is noted in CAM6-CTL. The observed afternoon peak at MAO is missed by CAM6-CTL. Instead, it shows a diurnal precipitation maximum at around 1100 LST. With the dCAPE-ULL trigger, CAM6-Trig reproduces the observed early-afternoon peak, but the amplitude is too weak. Different from the results at SGP, the DCP at MAO is much better simulated in E3SMv2-CAPETrig than that in E3SMv2. The observed early-afternoon rainfall maximum is well captured by E3SMv2-CAPETrig, with a secondary peak around midnight. In contrast, there is no clear diurnal variation in E3SMv2. The simulated precipitation is overestimated at night but underestimated in the afternoon compared to the observations. A further analysis suggests that the change in the air parcel starting launch level from two levels above the bottom model level in E3SMv1 to just one level above in E3SMv2 has affected the dCAPE-ULL performance, in particular for daytime precipitation. While the timing of the observed afternoon precipitation peak is well captured by TaiESM1, the simulated precipitation intensity is lower compared to the ARM observations. Both CMCGEM and ECMWF-IFS show a diurnal precipitation peak at around 1600-1700 LST, a few

552 hours later than the ARM observations. In addition, the maximum precipitation intensity is largely
553 overestimated in ECMWF-IFS.

554 Correspondingly, results from the hindcast runs during the second intensive operational
555 periods (IOPs, dry seasons, September 01 – October 14, 2014) of the GOAmazon field campaign
556 are shown in Figure 8b. Different from the SGP case, there is no clear improvement seen in the
557 hindcast runs compared to the climate simulations. In fact, most of the models even show worse
558 performance in their hindcast runs. For example, the simulated DCP from both UMGA7 and
559 UMGA8 compare better to the observations in their climate runs than in the hindcast runs. Both
560 UMGA7 and UMGA8 show a diurnal precipitation maximum peaking around noon, different from
561 the observed precipitation peak in the early afternoon. Similar results are also noted in the hindcast
562 runs of TaiESM1, with earlier rain peak time and lower maximum rain rate. Precipitation is too
563 weak in both E3SMv2-CAPETrig and E3SMv2 hindcasts, with the diurnal precipitation maximum
564 less than 2 mm/day in both models. For CMCGEM, both the climate runs and the hindcasts show
565 a diurnal precipitation peak at around 1600 LST but the bias in precipitation magnitude is even
566 larger in the hindcast runs. The only exception is ECMWF-IFS. Compared with its climate runs,
567 the hindcast runs of ECMWF-IFS show significant improvement in both the peak time and
568 maximum rain rate of DCP. This implies that the above-noted bias in the climate runs of ECMWF-
569 IFS could be attributed to the spurious moisture source in the semi-Lagrangian advection and the
570 large model time step of 2700 s.

571 The different model performances in hindcasts and climate simulations and over different
572 climate regimes highlights the challenge in capturing the diurnal variation in precipitation in
573 current weather and climate models. The model issue is not only related to the model physics, but
574 also related to the large-scale environments and the interactions between model physics and

575 dynamics. A hierarchic modeling framework helps test new developments of model convective
576 processes over different convective regimes to ensure the improvement is valid globally.
577
578 b. Individual afternoon rainfall events
579 Similar to SGP, the day-to-day comparisons between the hindcast runs and the ARM
580 observations during the dry seasons of the GOAmazon field campaign are displayed in Figure 9.
581 In this subsection, we will emphasize the days with afternoon precipitation maxima. Here, 13
582 afternoon precipitation days are selected from the ARM observations, following the criteria of
583 Tang et al. (2022). An afternoon precipitation day is defined as having 1) peak rain rate greater
584 than 1 mm/day, 2) rain peak time between 1100 and 2000 LST, 3) peak rain rate 1.5 times greater
585 than any rain rate beyond the period between 1100 and 2000 LST, and (4) it must fall into the
586 locally driven convection case library visually selected from radar and satellite images (Tian et al.,
587 2021).
588 Overall, ECMWF-IFS compares the best to the ARM observations, similar to earlier
589 discussion. About 80% (10 out of 13) of the observed afternoon precipitation days are correctly
590 simulated as afternoon precipitation days in ECMWF-IFS. The afternoon convection regime
591 during the GOAmazon dry seasons is also reasonably captured by CMCGEM, UMGA7, and
592 UMGA8, with a hit rate of 69%, 62%, and 62%, respectively. While TaiESM1 performs pretty
593 well in capturing the nocturnal precipitation days during PECAN, it misses the majority of the
594 observed afternoon precipitation days in the 2nd IOP of the GOAmazon experiment. Further
595 analysis indicates that the wrong cases in TaiESM1 are mainly attributed to days that do not exhibit
596 peak rain rate 1.5 times greater than any rain rate outside of 1100 to 2000 LST. More specifically,
597 about 67% of the wrong cases in TaiESM1 fulfill the first two criteria but fail the third criterion in

598 the definition of the ARM-observed afternoon precipitation days described above. The observed
599 afternoon precipitation days are generally poorly simulated in both E3SMv2 and E3SMv2-
600 CAPETrig. Statistically, 50% of the wrong cases in E3SMv2-CAPETrig are attributed to
601 precipitation peaking too early (before 1100 LST); while the wrong cases in E3SMv2 are largely
602 (54%) contributed by a diurnal precipitation maximum peaking during the nighttime (after 2000
603 LST).
604
605 **5. Discussions and conclusions**
606 Accurate simulation of diurnal precipitation continues to be an ongoing challenge for
607 GCMs, particularly over land. Problems in simulating the DCP are primarily due to deficiencies
608 in representing convection initiation, evolution, and propagation, as well as the interaction between
609 convection and its large-scale atmospheric environment and the underlying land surface. In this
610 study, the simulation of the DCP in participating GCMs is evaluated using both 8-year AMIP-type
611 climate runs and 5-day hindcasts for the ARM PECAN and GOAmazon field campaigns initialized
612 with NWP analyses. Particularly, we focus on the DCP at the ARM SGP and MAO sites,
613 representative of midlatitude and tropical land, respectively.
614 Common model biases are noted in the GCM climate runs, such as the excessive
615 precipitation over the tropics, the too frequent light rain, and the missing propagating convection
616 systems in the central U.S. At the SGP, the precipitation intensity is largely underestimated by all
617 participating GCMs in the climate runs, but this bias is noticeably improved in the hindcast runs.
618 This indicates that the too weak rainfall intensity in the climate runs may be due to errors in the
619 large-scale circulation and surface conditions (e.g., soil moisture) and the interaction between
620 convection and its environment. In addition, the timing of the simulated diurnal peak is largely

improved from the climate runs to hindcast runs. The observed nocturnal precipitation peak, missed by most models in the climate runs, is reasonably well captured in the hindcasts. This suggests that a well constrained large-scale condition is critical for GCMs to correctly simulate the DCP at the SGP. Different from the SGP, the GCM hindcasts show no clear improvement at the MAO. The model bias of both peak rain rate and its timing in the GCM climate runs persists in the corresponding hindcast runs.

The impact of model physics on the simulated DCP is examined by comparing models with different versions or physical parameterizations. In general, models that incorporate the role of the large-scale environment in convective triggering processes, such as ECMWF-IFS, E3SMv2, and CAM6-Trig, are able to improve the phase-lock issue in many GCMs where precipitation peaks near noon due to the unrealistically strong coupling of convection with surface heating over land. Models that allow convection to be decoupled from the boundary layer, such as ECMWF-IFS, E3SMv2, CAM6-Trig, and TaiESM, show capabilities in capturing nocturnal precipitation which is often associated with propagation of mesoscale systems. The convective memory introduced in UMGA8 helps reduce the overestimation of the frequency of light-to-moderate rain in the tropics while promoting intense rainfall events. But its impact is in general minor in the mean precipitation and DCP over both SGP and MAO. In fact, it actually acts to reduce the diurnal variation as precipitation events tend to maintain longer with memory.

Results from this study suggest that the DCP biases of low-resolution climate models cannot be fully resolved by simply increasing model resolutions as long as cumulus parameterizations are used in the model simulations. To better address the impact of model resolution on the simulated DCP, studies based on the intercomparisons of Cloud Permitting Models (CPMs) are needed. Current weather and climate models continue having difficulties in

capturing the diurnal variations of precipitation. As shown, different model performances are noted in hindcasts and climate simulations and over different climate regimes. The simulated DCP is the result of the interaction between model physics, the large-scale environment and the physics-dynamics coupling. The hierarchy modeling framework applied in the GASS-DCP project has been proven very useful to identify strengths and weaknesses of model parameterizations and test new approaches to simulate convective processes in different convective regimes.

Acknowledgement

This work is part of the GEWEX Global Atmospheric System Study (GASS) Panel's Diurnal Cycle of Precipitation Project. Work at LLNL is supported by the Earth and Environmental System Modeling, Regional and Global Model Analysis, Atmospheric System Research and Atmospheric Radiation Measurement programs, funded by the U.S. Department of Energy, Office of Science, Office of Biological and Environmental Research, LLNL Laboratory Directed Research and Development project 22-ERD-013, and is performed under the auspices of the U.S. DOE by LLNL under Contract DE-AC52-07NA27344. Pacific Northwest National Laboratory (PNNL) is operated for DOE by Battelle under contract DE-AC05-76RL01830. The work of K. Van Weverberg was supported by the Met Office Weather and Climate Science for Service Partnership (WCSSP) southeast Asia as part of the Newton Fund. The work of Yi-Chi Wang is supported by the National Science and Technology Council, Taiwan under MOST111-2111-M-001-013. The work of J. D. Neelin is supported by AGS-1936810.

References

Buehner, M., McTaggart-Cowan, R., Beaulne, A., Charette, C., Garand, L., Heillette, S., Lapalme, E., Laroche, S., Macpherson, S. R., Morneau, J., and Zadra,

A. (2015). Implementation of deterministic weather forecast systems based on ensemble-variational data assimilation at Environment Canada. Part I: The global system. *Monthly Weather Review*, **143**, 2532– 2559.

Covey, C., Gleckler, P. J., Doutriaux, C., Williams, D. N., Dai, A., Fasullo, J., Trenberth, K., and Berg, A. (2016). Metrics for the diurnal cycle of precipitation: Toward routine benchmarks for climate models. Journal of Climate, 29(12), 4461– 4471.

Cui, Z., Wang, Y., Zhang, G. J., Yang, M., Liu, J., and Wei, L. (2022). Effects of Improved Simulation of Precipitation on Evapotranspiration and Its Partitioning Over Land, Geophysical Research Letters.

Dai, A., Trenberth, K. E., and Karl, T. R. (1999). Effects of Clouds, Soil Moisture, Precipitation, and Water Vapor on Diurnal Temperature Range, *Journal of Climate*, *12*(8), 2451-2473.

Dai, A., and Trenberth, K. E. (2004). The diurnal cycle and its depiction in the Community Climate System Model. *Journal of Climate*, 17, 930–951.

Dai, A. (2006). Precipitation characteristics in eighteen coupled climate models. *Journal of Climate*, 19, 4605–4630. https://doi.org/10.1175/JCLI3884.1.

Dai, A., Lin, X., and Hsu, K.-L. (2007). The frequency, intensity, and diurnal cycle of precipitation in surface and satellite observations over low-and mid-latitudes. Climate Dynamics, 29, 727–744.

Daleu, C. L., Plant, R. S., Woolnough, S. J., Stirling, A. J., & Harvey, N. J. (2020). Memory properties in cloud-resolving simulations of the diurnal cycle of deep convection. Journal of Advances in Modeling Earth Systems, 12, e2019MS001897.

Danabasoglu, G., Lamarque, J.-F., Bacmeister, J., Bailey, D. A., DuVivier, A. K., and et al. (2020). The Community Earth System Model Version 2 (CESM2), Journal of Advances in Modeling Earth Systems.

Eyring, V., Bony, S., Meehl, G., Senior, C., Stevens, B., Stouffer, R., Taylor, K. (2016). Overview of the coupled model intercomparison project phase 6 (CMIP6) experimental design and organization. Geoscience Model Development, 9:1937–1958.

Fiedler, S., Crueger, T., D'Agostino, R., Peters, K., Becker, T., Leutwyler, D., Paccini, L., Burdanowitz, J., Buehler, S.A., Cortes, A.U., Dauhut, T., Dommenget, D., Fraedrich, K., Jungandreas, L., Maher, N., Naumann, A.K., Rugenstein, M., Sakradzija, M., Schmidt, H., Sielmann, F., Stephan, C., Timmreck, C., Zhu, X.H. and Stevens, B. (2020). Simulated tropical precipitation assessed across three major phases of the Coupled Model Intercomparison Project (CMIP). Monthly Weather Review, 148, 3653– 3680. https://doi.org/10.1175/mwr-d-19-0404.1.

Geerts, B., Parsons, D., Zieglgler, C. L., Weckwerth, T. M., Biggggerstaff, M. I., Clark, R. D., Coniglio, M. C., Demoz, B. B., Ferrare, R. A., Gallus, W. A. Jr., Haghi, K., Hanesiak, J. M., Klein, P. M., Knupp, K. R., Kosiba, K., McFarquhar, G. M., Moore, J. A., Nehrir, A. R., Parker,

M. D., Pinto, J. O., Rauber, R. M., Schumacher, R. S., Turner, D. D., Wang, Q., Wang, X., Wang, Z., & Wurman, J. (2017). The 2015 plains elevated convection at night field project. Bulletin of the American Meteorological Society, 98(4), 767– 786. https://doi.org/10.1175/BAMS-D-15-00257.1

Golaz, J.-C., Van Roekel, L. P., Zheng, X., Roberts, A., Wolfe, J. D., Lin, W., Bradley, A., Tang, Q., and et al. (2022). The DOE E3SM Model Version 2: Overview of the physical model, Earth and Space Science Open Archive, p. 61.

Good S, Fiedler E, Mao C, Martin MJ, Maycock A, Reid R, Roberts-Jones J, Searle T, Waters J, While J, Worsfold M. The Current Configuration of the OSTIA System for Operational Production of Foundation Sea Surface Temperature and Ice Concentration Analyses. Remote Sensing. 2020; 12(4):720. https://doi.org/10.3390/rs12040720.

Hersbach, H, Bell, B, Berrisford, P, et al. (2020). The ERA5 global reanalysis. Q J R Meteorol Soc.; 146: 1999– 2049. https://doi.org/10.1002/qj.3803.

Huffman, G. J., and coauthors (2007). The TRMM multisatellite precipitation analysis (TMPA): Quasi-global, multiyear, combined-sensor precipitation estimates at fine scales. J. Hydrometeor., 8, 38–55.

Huffman, G. J., D. T. Bolvin, D. Braithwaite, K. Hsu, R. Joyce, and P. Xie, (2019). Algorithm Theoretical Basis Document (ATBD) version 5.2 for the NASA Global Precipitation Measurement (GPM) Integrated Multi-satellite Retrievals for GPM (I-MERG). NASA GPM, 38 pp.

Jiang, X., Lau, N.-C., & Klein, S. A. (2006). Role of eastward propagating convection systems in the diurnal cycle and seasonal mean of summertime rainfall over the U.S. Great Plains. Geophysical Research Letters, 33, L19809. https://doi.org/10.1029/2006GL027022.

Joyce, R. J., J. E. Janowiak, P. A. Arkin, and P. Xie, (2004). CMORPH: A method that produces global precipitation estimates from passive microwave and infrared data at high spatial and temporal resolution. J. Hydrometeor., 5, 487–503.

Kikuchi, K., and Wang, B. (2008). Diurnal precipitation regimes in the global tropics. *Journal of Climate*, 21, 2680–2696, https://doi.org/10.1175/2007JCLI2051.1.

Klein, S. A., Jiang, X., Boyle, J., Malyshev, S., & Xie, S. (2006). Diagnosis of the summertime warm and dry bias over the US Southern Great Plains in the GFDL climate model using a weather forecasting approach. Geophysical Research Letters, 33(18), L18805. https://doi.org/10.1029/2006gl027567.

Ma, H.-Y., Klein, S. A., Lee, J., Ahn, M.-S., Tao, C., and Gleckler, P. J. (2022). Superior daily and sub-daily precipitation statistics for intense and long-lived storms in global storm-resolving models. Geophysical Research Letters, 49, e2021GL096759.

Ma, H.-Y., Zhou, C., Zhang, Y., Klein, S. A., Zelinka, M. D., Zheng, X., Xie, S., Chen, W.-T., & Wu, C.-M. (2021). A multi-year short-range hindcast experiment with CESM1 for evaluating

climate model moist processes from diurnal to interannual timescales. Geoscientific Model Development, 14(1), 73–90. https://doi.org/10.5194/gmd-14-73-2021.

Ma, H.-Y., Klein, S. A., Xie, S., Zhang, C., Tang, S., Tang, Q., et al. (2018). CAUSES: On the role of surface energy budget errors to the warm surface air temperature error over the Central U.S. Journal of Geophysical Research: Atmospheres, 123, 2888– 2909. https://doi.org/10.1002/2017jd027194.

Ma, H.-Y., and Coauthors. (2015). An improved hindcast approach for evaluation and diagnosis of physical processes in global climate models. J. Adv. Model. Earth Syst., 7, 1810–1827, https://doi.org/10.1002/2015MS000490.

Ma, H.-Y., et al. (2014), On the correspondence between mean forecast errors and climate errors in CMIP5 models, J. Clim., 27, 1781–1798.

Ma, H.-Y., S. Xie, J. S. Boyle, S. A. Klein, and Y. Zhang (2013), Metrics and diagnostics for precipitation-related processes in climate model short-range hindcasts, J. Clim., 26, 1516–1534.

Martin, S. T., Artaxo, P., Machado, L. A. T., Manzi, A. O., Souza, R. A. F., Schumacher, C., Wang, J., Andreae, M. O., Barbosa, H. M. J., Fan, J., Fisch, G., Goldstein, A. H., Guenther, A., Jimenez, J. L., Pöschl, U., Silva Dias, M. A., Smith, J. N., and Wendisch, M.: Introduction: Observations and Modeling of the Green Ocean Amazon (GoAmazon2014/5), Atmos. Chem. Phys., 16, 4785–4797, https://doi.org/10.5194/acp-16-4785-2016, 2016.

Martinez-Villalobos, C., Pendergrass, A. G. & Neelin, J. D. (2022). Metrics for evaluating CMIP6 representation of daily precipitation probability distributions. J. Climate, 35, 5719-5743, doi:10.1175/JCLI-D-21-0617.1.

Martinez-Villalobos and Neelin, J. D. (2021). Climate models capture key features of extreme precipitation probabilities across regions. Environ. Res. Lett. 16, 024017.

McTaggart-Cowan, R., P.A. Vaillancourt, A. Zadra, S. Chamberland, M. Charron, S. Corvec, J.A. Milbrandt, D. Paquin-Ricard, A. Patoine, M. Roch, L. Separovic, and J. Yang, 2019a: Modernization of atmospheric physics in Canadian NWP. *J. Adv. Model. Earth Syst.*, **11**, 3593–3635, https://doi.org/10.1029/2019MS001781.

McTaggart-Cowan, R., Vaillancourt, P.A., Zadra, A., Separovic, L., Corvec, S., and Kirshbaum, D, 2019b. A Lagrangian perspective on parameterizing deep convection. *Monthly Weather Review*, 147(11), 4127-4149, https://doi.org/10.1175/MWR-D-19-0164.1

McTaggart-Cowan, R., P. A.Vaillancourt, L. Separovic, S. Corvec, and A. Zadra, 2020: A convection parameterization for low-CAPE environments. *Mon. Wea. Rev.*, **148(12)**, 4917–4941, https://doi.org/10.1175/MWR-D-20-0020.1.

Neale, R. B., Richter, J. H., and Jochum, M. (2008). The Impact of Convection on ENSO: From a Delayed Oscillator to a Series of Events, Journal of Climate.

Nesbitt, S. W., and Zipser, E. J. (2003). The diurnal cycle of rainfall and convective intensity according to three years of TRMM measurements. Journal of Climate, 16, 1456–1475.

Park, S. (2014). A unified convection scheme (UNICON). Part I: Formulation. Journal of the Atmospheric Sciences, 71(11), 3902– 3930. https://doi.org/10.1175/JAS-D-13-0233.1.

Phillips, T. J., and Coauthors. (2004). Evaluating parameterizations in general circulation models: Climate simulation meets weather prediction. Bull. Amer. Meteor. Soc., 85, 1903–1916, https://doi.org/10.1175/BAMS-85-12-1903.

Rasch, P. J., S. Xie, P. Ma, W. Lin, et al. (2019): An Overview of the Atmospheric Component of the Energy Exascale Earth System Model. Journal of Advances in Modeling Earth Systems, DOI:10.1029/2019MS001629.

Satoh, M., Stevens, B., Judt, F., Khairoutdinov, M., Lin, S., Putman, W. M., and Düben, P. (2019). Global cloud-resolving models. Current Climate Change Reports, 5(3), 172-184. https://doi.org/10.1007/s40641-019-00131-0.

Stevens, B., Satoh, M., Auger, L., Biercamp, J., Bretherton, C. S., Chen, X., et al. (2019). DYAMOND: The DYnamics of the atmospheric general circulation modeled on non-hydrostatic domains. Progress in Earth and Planetary Science, 6, 61.

Tang, S., Xie, S., Guo, Z., Hong, S.-Y. et al. (2022). Long-term single-column model intercomparison on diurnal cycle of precipitation over mid-latitude and tropical land. Quart J Roy Meteor Soc 1–29.

Tang, S., Gleckler, P., Xie, S., Lee, J., Ahn, M-S., Covey, C., and Zhang, C. (2021). Evaluating diurnal and semi-diurnal cycle of precipitation in CMIP6 models using satellite- and ground-based observations. Journal of Climate, 34(8):3189–3210.

Tang, S., Xie, S., Zhang, Y., Zhang, M, Schumacher, C., Upton, H., Jensen, M.P., Johnson, K.L., Wang, M., Ahlgrimm, M., Feng, Z., Minnis, P. and Thieman, M. (2016). Large-scale vertical velocity, diabatic heating and drying profiles associated with seasonal and diurnal variations of convective systems observed in the GoAmazon2014/5 experiment. Atmospheric Chemistry and Physics, 16, 14249– 14264. https://doi.org/10.5194/acp-16-14249-2016.

Tao, C., Xie, S., Tang, S., Lee, J., Ma, H.-Y., Zhang, C., and Lin, W. (2022). Diurnal cycle of precipitation over global monsoon systems in CMIP6 simulations. Climate Dynamics.

Tian, Y., Zhang, Y., Klein, S.A. and Schumacher, C. (2021). Interpreting the diurnal cycle of clouds and precipitation in the ARM GOAmazon observations: shallow to deep convection transition. Journal of Geophysical Research – Atmospheres, 126, e2020JD033766.

Tiedtke, M., 1989: A Comprehensive Mass Flux Scheme for Cumulus Parameterization in Large-Scale Models. Mon. Wea. Rev., 117, 1779–1800, https://doi.org/10.1175/1520-0493(1989)117<1779:ACMFSF>2.0.CO;2.

812 Wang, Y. C., Pan, H. L., & Hsu, H. H. (2015). Impacts of the triggering function of cumulus
813 parameterization on warm-season diurnal rainfall cycles at the Atmospheric Radiation
814 Measurement Southern Great Plains Site. Journal of Geophysical Research: Atmospheres, 120,
815 10,681– 10,702. https://doi.org/10.1002/2015JD023337.

816 Wang, Y., Zhang, G. J., Xie, S., Lin, W., Craig, G. C., Tang, Q., and Ma, H.-Y. (2021). Effects of
817 coupling a stochastic convective parameterization with the Zhang–McFarlane scheme on
818 precipitation simulation in the DOE E3SMv1.0 atmosphere model. Geoscientific Model
819 Development, 14, 1575– 1593. https://doi.org/10.5194/gmd-14-1575-2021.

820 Williams K.D., A. Bodas-Salcedo, M. Deque, S. Fermepin, B. Medeiros, M. Watanabe, C. Jakob,
821 S.A. Klein, C.A. Senior, and D.L. Williamson. (2013). The Transpose-AMIP II experiment and
822 its application to the understanding of Southern Ocean cloud biases in climate models. J.
823 Climate. 26 3258-3274 doi:10.1175/JCLI-D-12-00429.1.

824 Wong, M., G. Romine, and C. Snyder, 2020: Model Improvement via Systematic Investigation of
825 Physics Tendencies. Mon. Wea. Rev., 148, 671–688, https://doi.org/10.1175/MWR-D-19-
826 0255.1.

827 Xie, P., Joyce, R., Wu, S., Yoo, S. H., Yarosh, Y., Sun, F., & Lin, R. (2017). Reprocessed, bias-
828 corrected CMORPH global high-resolution precipitation estimates from 1998. Journal of
829 Hydrometeorology, 18, 1617–1641. https://doi.org/10.1175/JHM-D-16-0168.1.

830 Xie, S., Wang, Y.-C., Lin, W., Ma, H.-Y., Tang, Q., Tang, S., Zheng, X., Golaz, J.-C., Zhang, G.
831 J., and Zhang, M. (2019). Improved Diurnal Cycle of Precipitation in E3SM With a Revised
832 Convective Triggering Function, Journal of Advances in Modeling Earth Systems.

833 Xie, S., Lin, W., Rasch, P. J., Ma, P.-L., Neale, R., Larson, V. E., et al. (2018). Understanding
834 cloud and convective characteristics in version 1 of the E3SM atmosphere model. Journal of
835 Advances in Modeling Earth Systems, 10, 2618–2644.

836 Xie, S., Zhang, Y., Giangrande, S. E., Jensen, M. P., McCoy, R., & Zhang, M. (2014). Interactions
837 between cumulus convection and its environment as revealed by the MC3E sounding array.
838 Journal of Geophysical Research: Atmospheres, 119, 11,784– 11,808.

839 Xie, S., H.-Y. Ma, J. S. Boyle, S. A. Klein, and Y. Zhang (2012), On the correspondence between
840 short- and long-timescale systematic errors in CAM4/CAM5 for the years of tropical
841 convection, J. Clim., 25, 7937–7955.

842 Xie, S., Cederwall, R. T., and Zhang, M. (2004). Developing long-term single-column
843 model/cloud system resolving model forcing data using numerical weather prediction products
844 constrained by surface and top of the atmosphere observations. Journal of Geophysical
845 Research, 109, D01104. https://doi.org/10.1029/2003JD004045.

846 Xie, S., and M. H. Zhang, 2000: Impact of the Convection triggering Function on Single-Column
847 Model Simulations. J. Geophys. Res., 105, 14983-14996.

Yang, G.-Y. and Slingo, J. (2001). The Diurnal Cycle in the Tropics, Monthly Weather Review, 129, 784-801.

Zhang, G. and McFarlane, N. A. (1995). Sensitivity of climate simulations to the parameterization of cumulus convection in the Canadian climate center general circulation model, Atmosphere-Ocean.

Zhang, G. J., & Mu, M. (2005). Effects of modifications to the Zhang-McFarlane convection parameterization on the simulation of the tropical precipitation in the National Center for Atmospheric Research Community Climate Model, version 3. Journal of Geophysical Research, 110, D09109. https://doi.org/10.1029/2004JD005617.

Table 1. Participating models and their basic information.

Model name	Full name	Run type	Horizontal resolution	Vertical levels	Timestep	Contact Person
CAM6-CTL	*NCAR CAM6*	Climate	0.9°×1.25°	32	30m	Guang Zhang, Zeyu Cui
CAM6-Trig	*NCAR CAM6 with revised convection trigger*	Climate	0.9°×1.25°	32	30m	Guang Zhang, Zeyu Cui
*CMCGEM	*Canadian Meteorological Center Global Environmental Multiscale*	Climate, Hindcasts	Hindcasts: 15 km Climate: 39 km	84 (top at 0.1hPa)	Hindcasts: 450s Climate: 900s	Paul Vaillancourt, Jing Yang
*ECMWF-IFS	*ECMWF Integrated Forecast System*	Climate, Hindcasts	Hindcasts: 18 km Climate: 60 km	137	Hindcasts: 720s Climate: 2700s	Peter Bechtold
*E3SMv2	*E3SM version 2*	Climate, Hindcasts	1° (~110 km near equator)	72	30m	Shaocheng Xie, Hsi-Yen Ma
*E3SMv2-CAPETrig	*E3SMv2 with revised convective trigger turned off*	Climate, Hindcasts	1° (~110 km near equator)	72	30m	Same as above
MPAS	*Model for Prediction Across Scales*	Hindcasts	15 km	55	75s	May Wong
*TaiESM1	*Taiwan Earth System Model version 1*	Climate, Hindcasts	0.9°×1.25°	30	30m	Yi-Chi Wang
*UMGA7	*Unified Model Global Atmosphere (UMGA) version 7*	Climate, Hindcasts	N320 (440 km near equator)	70 (top at 80km)	12m	Kwinten Van Weverberg
*UMGA8	*UMGA version 8*	Climate, Hindcasts	Same as above	Same as above	Same as above	Same as above

* denotes the models that run both climate simulations and hindcasts.

Table 2. Model physics in the participating models

Model name	Turbulence	Stratiform clouds	Shallow convection	References	Contact Person
CAM6-CTL	CLUBB	MG2, CLUBB	CLUBB	Danabasoglu et al. (2020)	Guang Zhang, Zeyu Cui
CAM6-Trig	CLUBB	MG2, CLUBB	CLUBB	Danabasoglu et al. (2020) Cui et al. (2021)	Guang Zhang, Zeyu Cui
*CMCGEM	TKE = 1.5	Sundqvist scheme	Modified Bechtold et al. (2001)	McTaggart-Cowan et al. (2019a)	Paul Vaillancourt, Jing Yang
*ECMWF-IFS	K-diffusion	Prognostic cloud scheme (4 water species + cloud fraction)	Same as deep (see Table 2) only differs by entrainment and closure	https://www.ecmwf.int/en/publications/ifs-documentation	Peter Bechtold
*E3SMv2	CLUBB	MG2, CLUBB	CLUBB	Golaz et al. (2022)	Shaocheng Xie, Hsi-Yen Ma
*E3SMv2-CAPETrig	CLUBB	MG2, CLUBB	CLUBB	Same as above	Same as above
MPAS	MYNN	Thompson prognostic microphysics (non-aerosol-aware)	Scale-aware New Tiedtke	Skamarock et al. (2012) Nakanishi and Niino (2006, 2009) Olson et al. (2019) Thompson et al. (2008) Wang (2022)	May Wong
*TaiESM1	UW	MG, GTS (Shiu et al. 2021)	UW	Lee et al. (2019)	Yi-Chi Wang
*UMGA7	First-order turbulence closure (Lock et al. 2000) with modification described in Lock (2001) and Brown et al. (2008)	Macrophysics: Prognostic cloud fraction and prognostic condensate (PC2) scheme (Wilson et al., 2008a, b) Microphysics: Single-moment scheme based on Wilson and Ballard (1999)	Mass-flux convection scheme based on Gregory and Rowntree (1990)	Walters et al. (2019)	Kwinten Van Weverberg
*UMGA8	Same as above	Same as above	Same as above	Same as above	Same as above

* denotes the models that run both climate simulations and hindcasts.

Table 3. Deep convective parameterizations in the participating models.

Model name	Deep convection	Closure	Convective trigger	Downdraft	References
CAM6-CTL	ZM	Dilute CAPE	CAPE > 70 J/kg	Downdraft starts from the level of minimum moist static energy	Zhang and McFarlane (1995) Neale et al. (2008)
CAM6-Trig	ZM with revised trigger	Dilute CAPE	CAPE > 0; dCAPE > 45 J/kg/hr; allowing convective parcel to launch above PBL but below 600 hPa	Downdraft starts from the level of minimum moist static energy	Zhang and McFarlane (1995) Xie et al. (2019) Cui et al. (2021)
*CMCGEM	Mass flux	CAPE	Look for a 60 hPa mixed parcel, to which a flow-dependent temperature perturbation is added, in the lowest 300 hPa that is buoyant once lifted to the LCL	Starts at the level of minimum saturation equivalent potential temperature	Kain and Fritsch (1990, 1992) McTaggart-Cowan et al. (2019a, 2019b)
*ECMWF-IFS	Bulk mass flux	Dilute CAPE + moisture convergence	Simplified test ascent from all levels up to maximum 300 hPa, positive buoyancy at cloud base	Saturated, 0.3 updraft mass flux at level of free sink	Tiedtke (1989) Bechtold et al. (2004, 2008, 2014) Becker et al. (2021)
*E3SMv2	ZM with revised convective trigger	Dilute CAPE	dCAPE_ULL trigger: (1) CAPE > 0; (b) dCAPE > 0; (c) The air parcel launch level is chosen between the surface and 600 hPa	Downdraft starts from updraft-top mass flux	Xie et al. (2019) Zhang and McFarlane (1995)
*E3SMv2-CAPETrig	ZM	Dilute CAPE	CAPE trigger: (1) CAPE >70 J/kg; (2) The air parcel launch level is chosen within the boundary layer	Downdrafts starts from updraft-top mass flux	Xie et al. (2018) Zhang and McFarlane (1995)
MPAS	Scale-aware New Tiedtke	Relaxes CAPE to a value generated by the planetary boundary layer processes (Bechtold et al. 2014)	CAPE exists in an entraining ascending air parcel with cloud depth exceeding 2 km	Downdrafts are driven by precipitation evaporation in the updrafts and originate at the level of free sink	Tiedtke (1989) Bechtold et al. (2008, 2014) Zhang and Wang (2017) Wang (2022)
*TaiESM1	ZM + ULL + CIN	Dilute CAPE	ULL: The air parcel launch level is chosen between the surface and 600 hPa CIN: convective inhibition estimated by difference between launching level and LFC < 150 hPa	Downdraft starts from updraft-top mass flux	Wang et al. (2015) Zhang and McFarlane (1995)
*UMGA7	Mass-flux convection scheme based on Gregory and Rowntree (1990)	CAPE: closure based on Fritsch and Chappell (1980)	The diagnosis of shallow and deep convection is based on an undilute parcel ascent from the near surface for grid boxes where the surface buoyancy flux is positive and forms part of the boundary-layer diagnosis (Lock et al., 2000)	Gregory and Allen (1991)	Gregory and Rowntree (1990) Gregory and Allen (1991) Walters et al. (2019)
*UMGA8	Same as above	Same as above	Similar to the above but with the prognostic entrainment to introduce convective memory in the model.	Same as above	Gregory and Rowntree (1990) Gregory and Allen (1991) Willett et al. (in preparation)

* denotes the models that run both climate simulations and hindcasts.

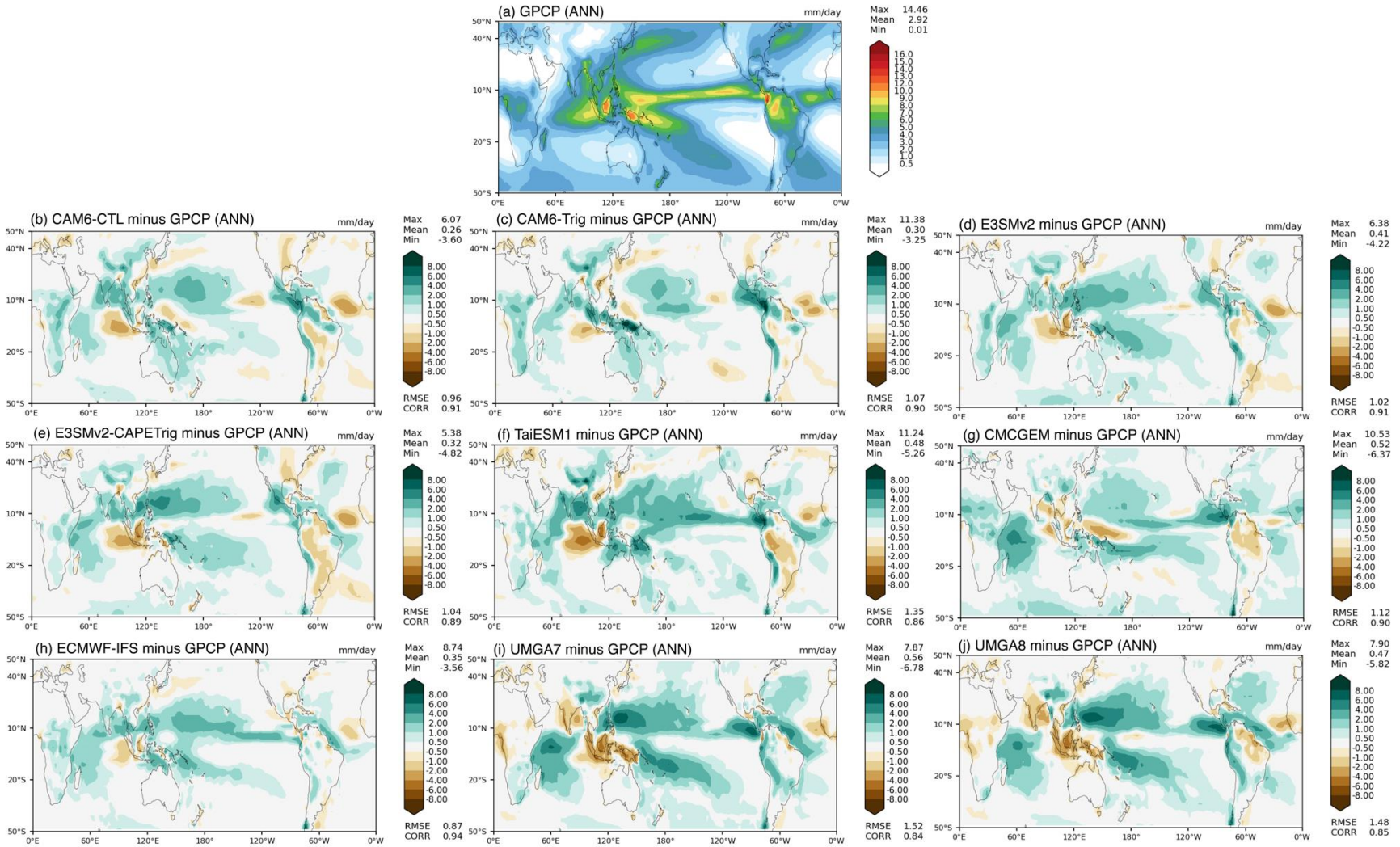

Figure 1. Annual mean precipitation rate (mm/day): (a) GPCP observational estimate, model bias from (b) CAM6-CTL, (c) CAM6-Trig, (d) E3SMv2, (e) E3SMv2-CAPETrig, (f) TaiESM1, (g) CMCGEM, (h) ECMWF-IFS, (i) UMGA7, and (j) UMGA8. RMSE, root-mean-square error. CORR, linear correlation coefficient between observation and model.

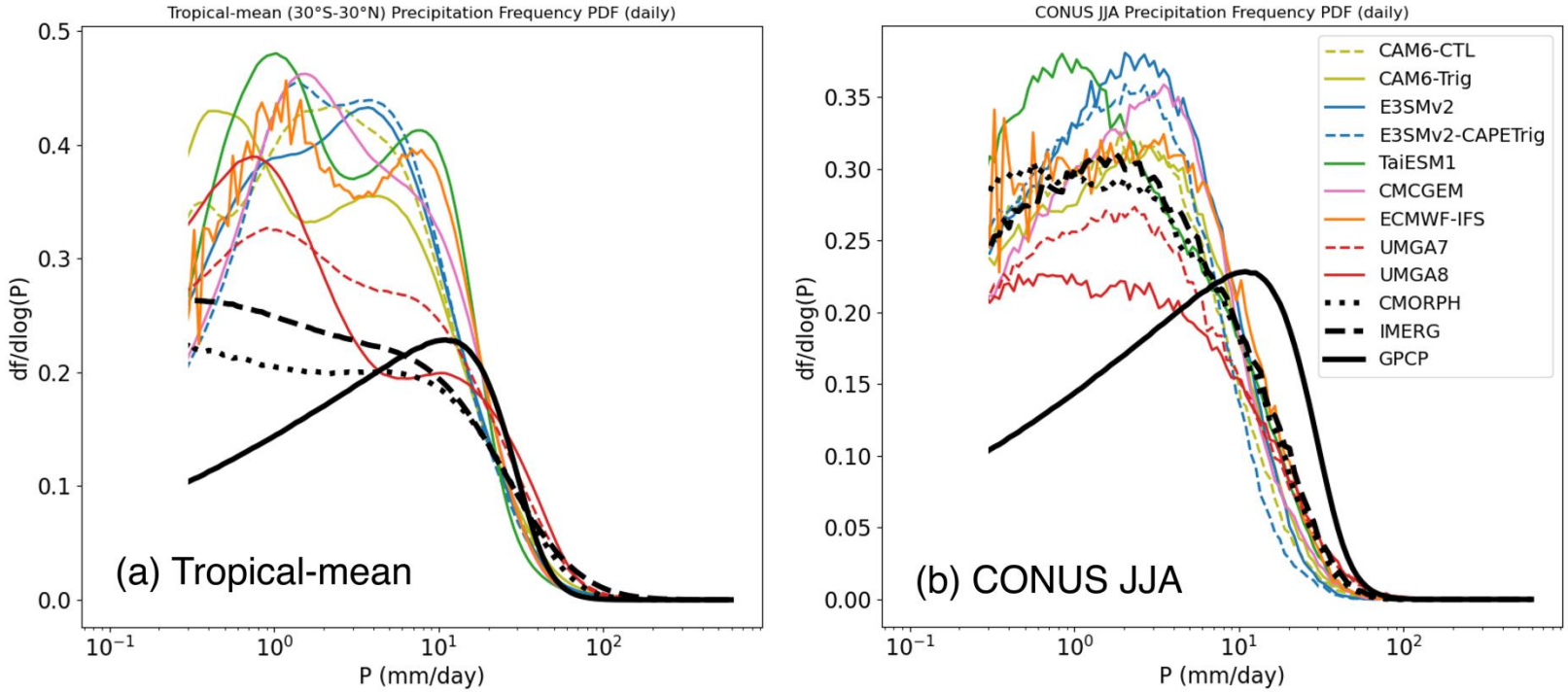

Figure 2. Daily mean precipitation frequency (unit: dF/dlog(P)) functions of total precipitation for the GPCP (black, solid), CMORPH (black, dotted) and IMERG (black, dashed) observations and model simulations (colored) for (a) annual mean over the tropics (30°S-30°N), and (b) June-July-August mean over CONUS. The precipitation rates (unit: mm/day) are firstly averaged over daily intervals. The frequency distribution is then derived by combining data from all the grid boxes at 1° × 1° resolution without any further averaging. The x axis bin edges are specified as $x_n + 1/x_n = 1.07$ to ensure an equal space of log10(1.07) in the logarithm scale, starting at 0.1 mm/day and ending at 617.3 mm/day. The frequency values are normalized by the x interval. Results are only shown up to 0.3 mm/day due to the data uncertainties.

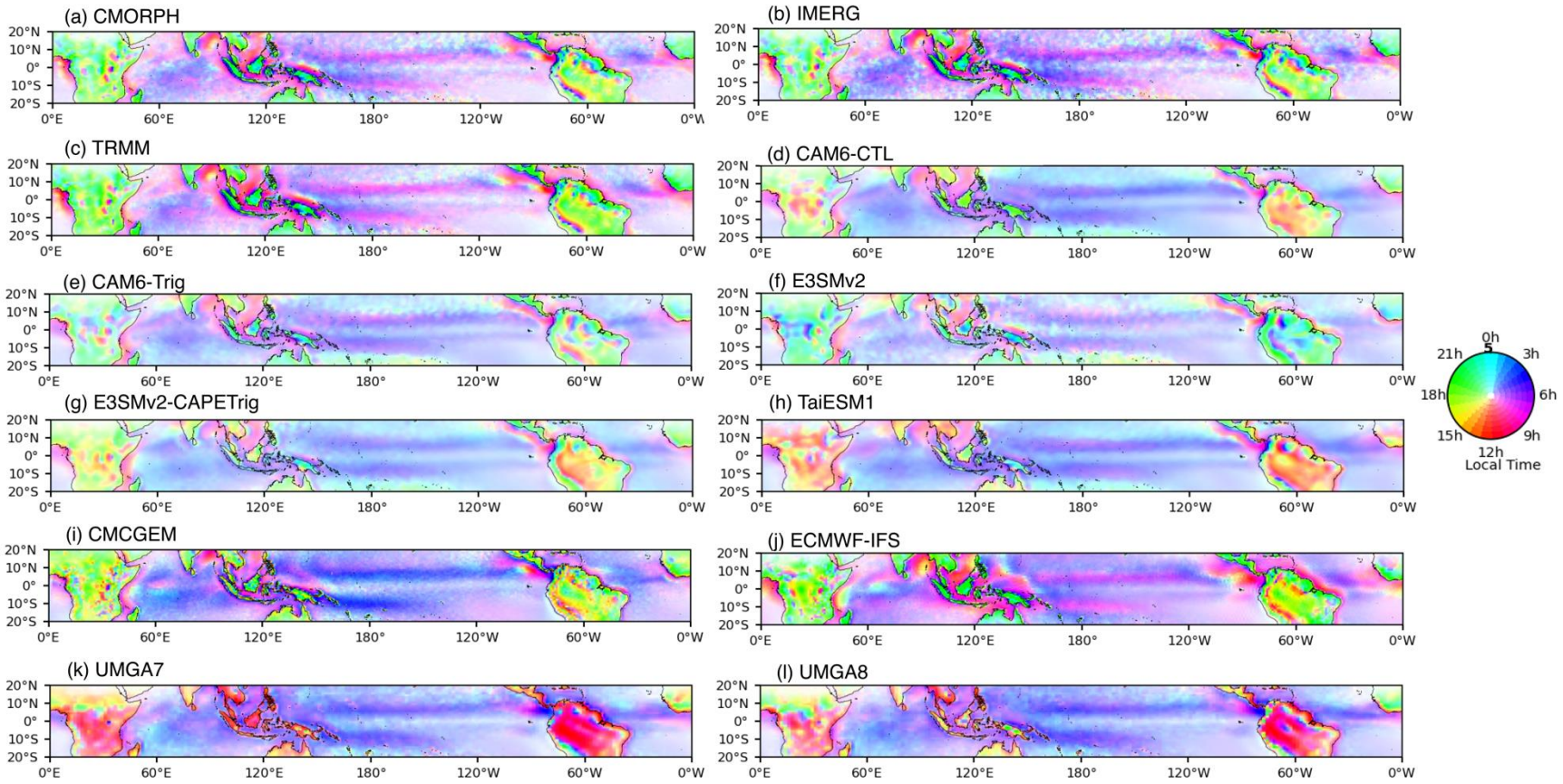

Figure 3. Annual mean time phase (color) and amplitude (color density) of the first diurnal harmonic of total precipitation (mm/day) from (a) CMORPH, (b) IMERG, (c) TRMM, (d) CAM6-CTL, (e) CAM6-Trig, (f) E3SMv2, (g) E3SMv2-CAPETrig, (h) TaiESM1, (i) CMCGEM, (j) ECMWF-IFS, (k) UMGA7, and (l) UMGA8.

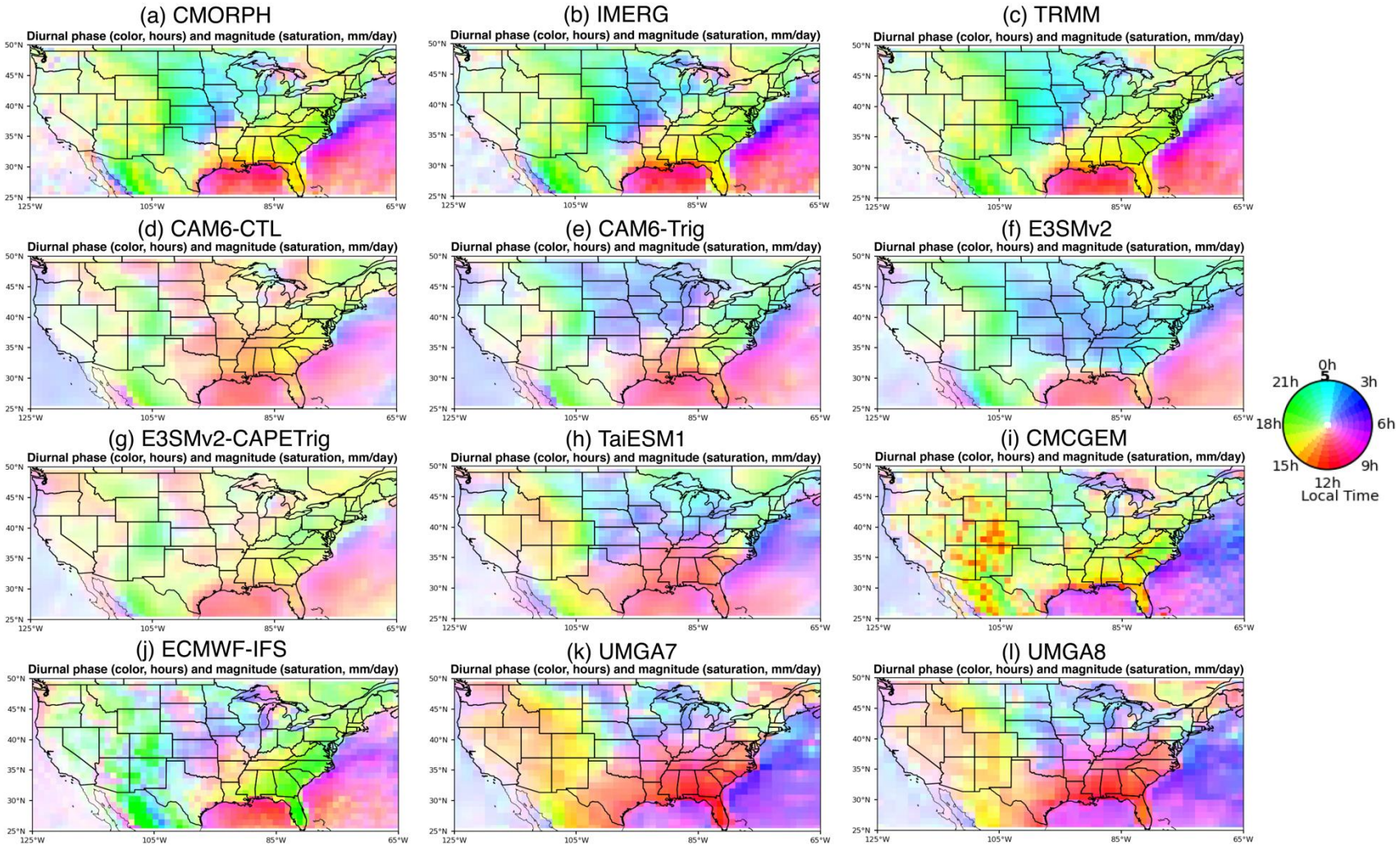

Figure 4. Same as Figure 3 except for the contiguous United States in June-July-August season.

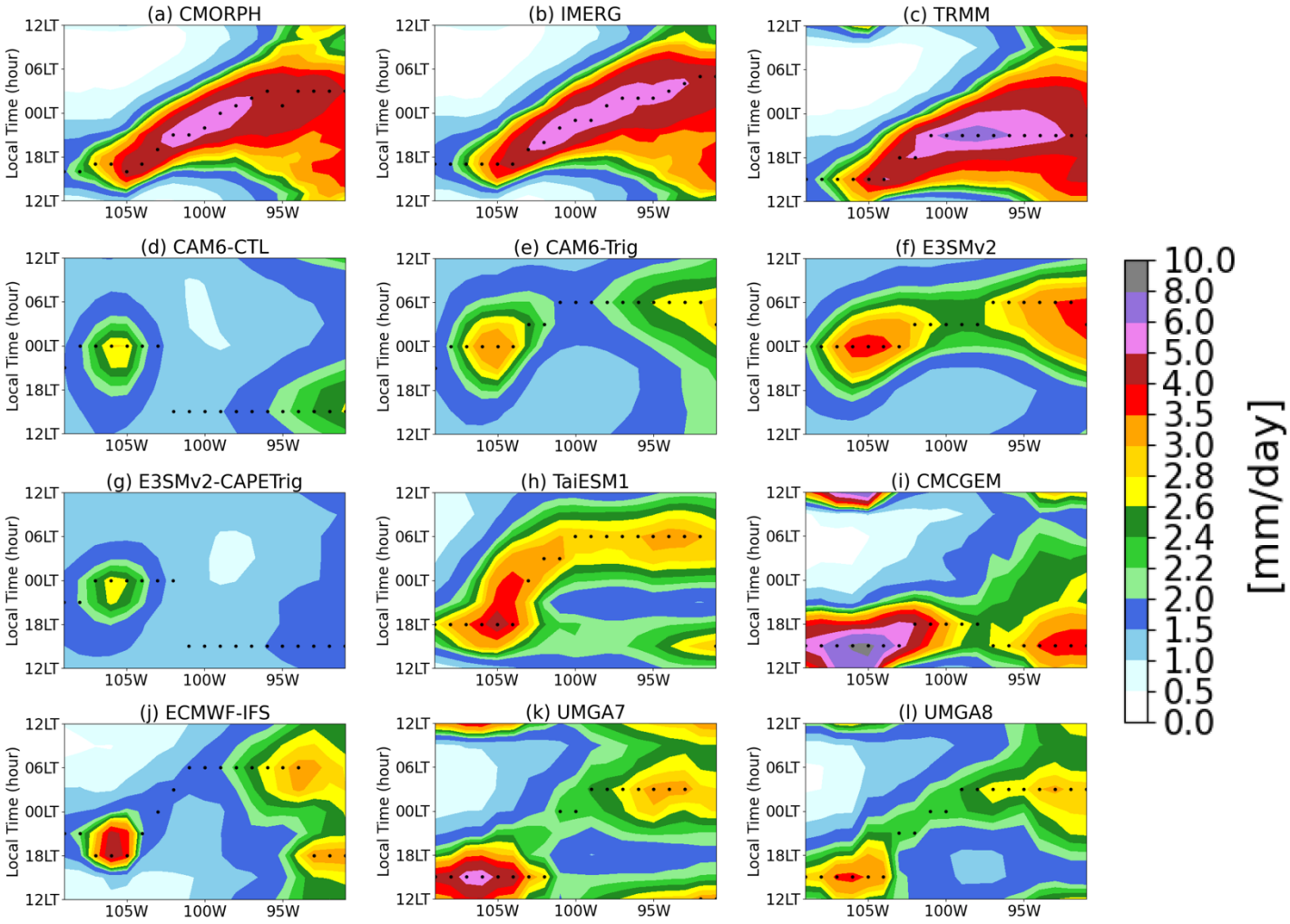

Figure 5. Diurnal and longitudinal (averaged from 35°-45°N) distribution of precipitation over the central U.S. from (a) CMORPH, (b) IMERG, (c) TRMM, (d) CAM6-CTL, (e) CAM6-Trig, (f) E3SMv2, (g) E3SMv2-CAPETrig, (h) TaiESM1, (i) CMCGEM, (j) ECMWF-IFS, (k) UMGA7, and (l) UMGA8 averaged over June-July-August of 2011-2018. The black dots denote the rain peak time for each longitudinal position.

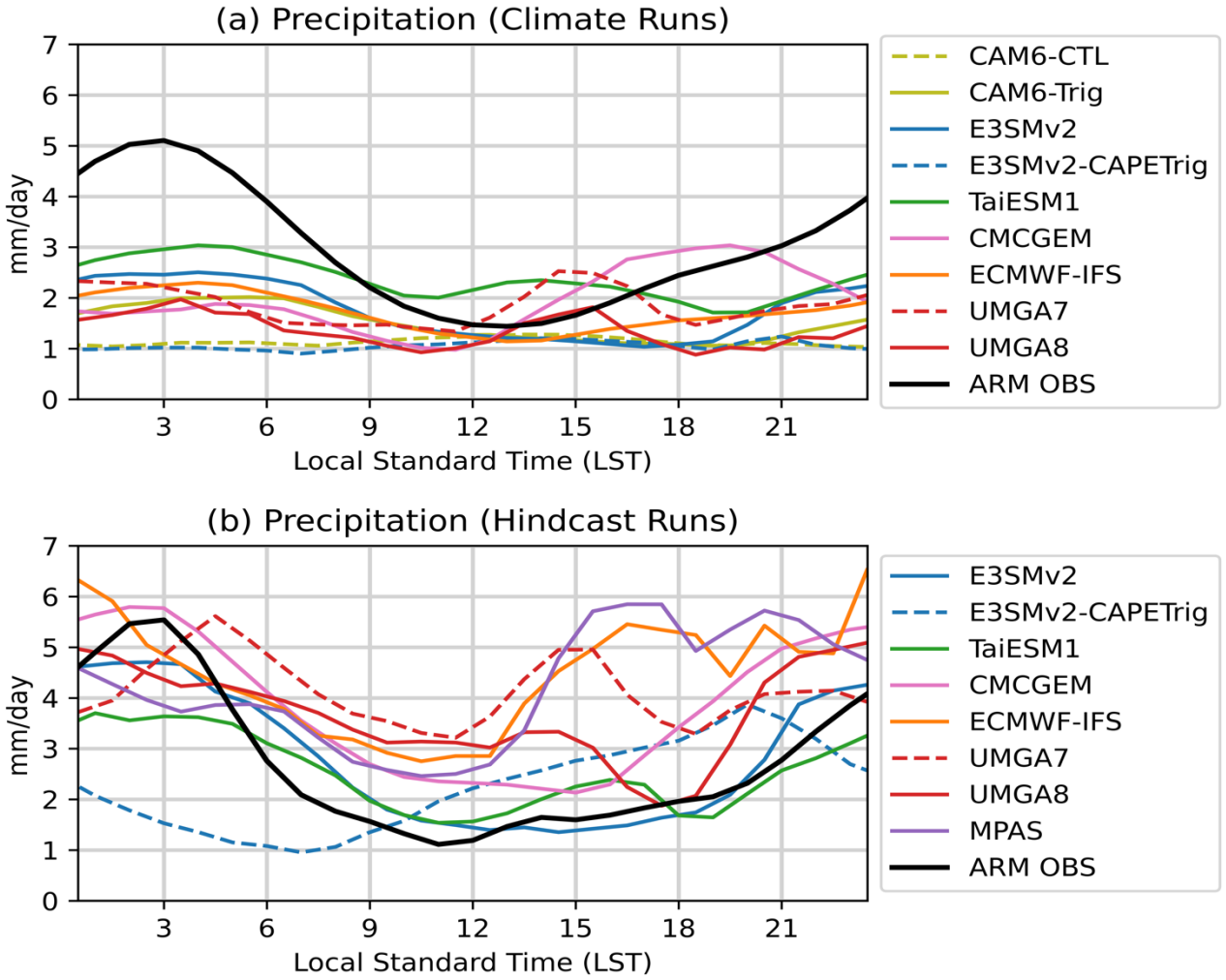

Figure 6. The composite mean diurnal cycle of precipitation (mm/day) for (a) climate runs (June-August, 2011-2018) and (b) hindcast runs (June 01 – July 15, 2015). Results from the 5-day hindcasts are averaged over Day 2 to Day 5 hindcast lead time. Domain-mean precipitation measurements from the ARM continuous forcing data set and the VARANAL for PECAN are used in (a) and (b), respectively.

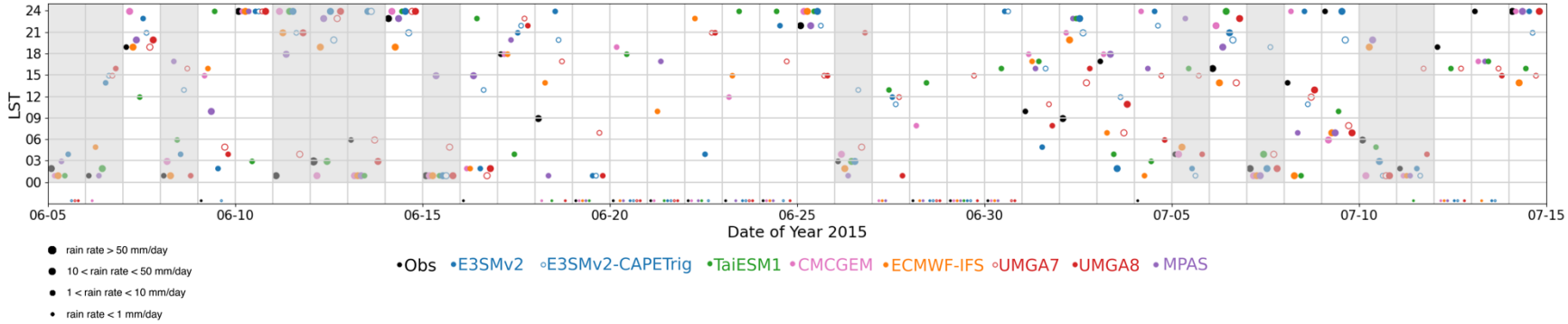

Figure 7. Peak rain rate (unit: mm/day) and rain peak time (LST) for each day during the PECAN field campaign. The 12 nocturnal precipitation days selected from the ARM observations are highlighted with gray-shaded areas. The rain peak time is only shown for days with peak rain rate greater than 1 mm/day. Definitions of nocturnal precipitation days are described in section 4.1.

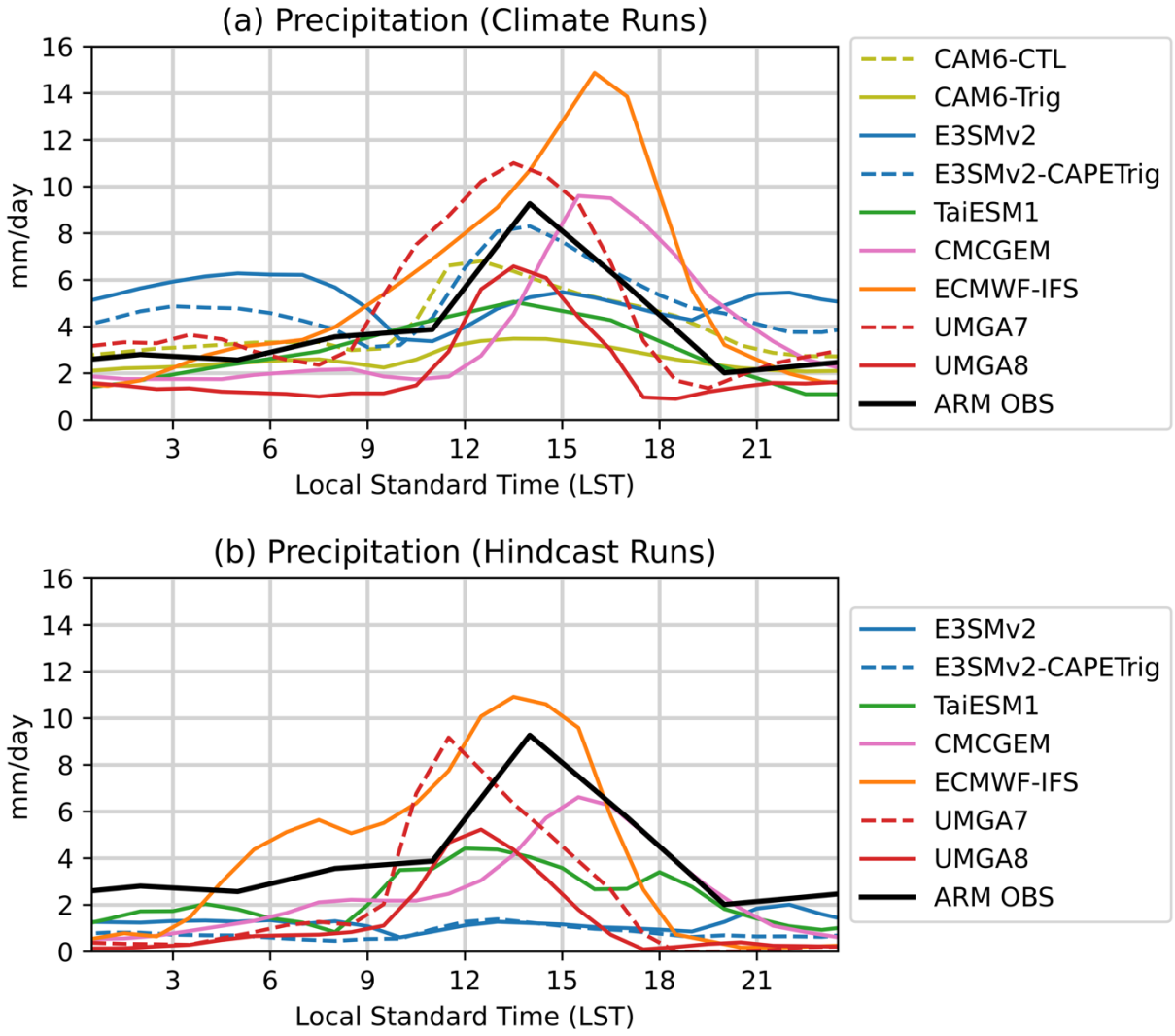

Figure 8. The composite mean diurnal cycle of precipitation (mm/day) for (a) climate runs (September-October, 2011-2018) and (b) hindcast runs (September 01 – October 14, 2014). Results from the 5-day hindcasts are averaged over Day 2 to Day 5 hindcast lead time.

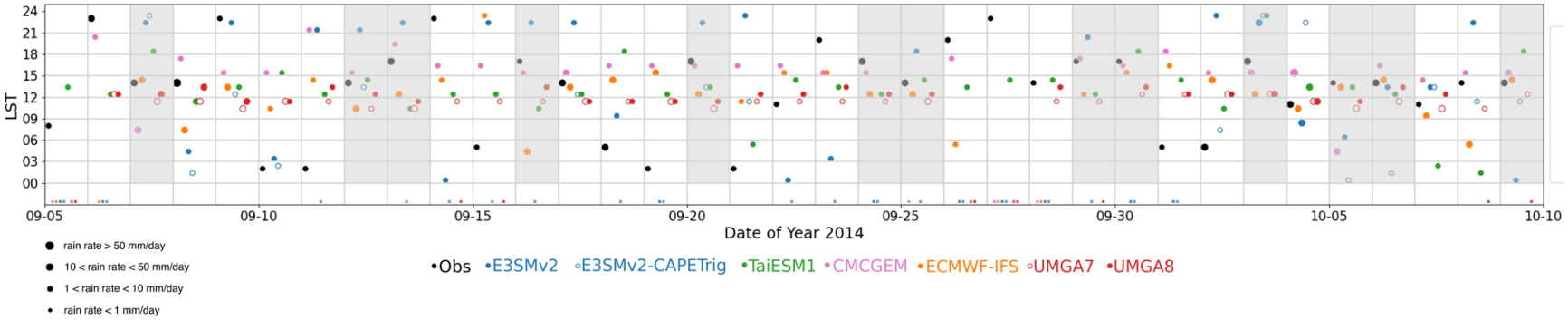

Figure 9. Peak rain rate (unit: mm/day) and rain peak time (LST) for each day during the 2nd IOP of the GOAmazon field campaign. The 13 afternoon precipitation days selected from the ARM observations are highlighted with gray-shaded areas. The rain peak time is only shown for days with peak rain rate greater than 1 mm/day. Definitions of afternoon precipitation days are described in section 4.2.